NASA CR-176,237

NASA-CR-176237
19860000547

A Reproduced Copy

OF

NASA CR-176,237

Reproduced for NASA

by the

NASA Scientific and Technical Information Facility

LIBRARY COPY

JUN 2 1986

LANGLEY RESEARCH CENTER
LIBRARY, NASA
HAMPTON, VIRGINIA

FFNo 672 Aug 65

NF00462

THE ROLE OF FREESTREAM TURBULENCE SCALE IN SUBSONIC FLOW SEPARATION

J. Leith Potter, Co-Principal Investigator
W. R. Seebaugh, Co-Principal Investigator
Carl E. Fisher, Graduate Student
R. Joel Barnett, Graduate Student
Rajiv B. Gokhale, Graduate Student

Sponsored Research Project RG-5997
NASA Research Grant NAG-1-483

Interim Progress Report 2

Period Covered: 1 January 1985 - 30 June 1985

(NASA-CR-176237) THE ROLE OF FREESTREAM TURBULENCE SCALE IN SUBSONIC FLOW SEPARATION Interim Progress Report, 1 Jan. - 30 Jun. 1985 (Vanderbilt Univ.) 56 p HC A04/MF A01 CSCL 01A G3/02
N86-10014
Unclas 15818

VANDERBILT UNIVERSITY
School of Engineering
Department of Mechanical & Materials Engineering
Nashville TN 37235

OCT 1985
RECEIVED
NASA STI FACILITY
ACCESS DEPT.

N86-10014

THE ROLE OF FREESTREAM TURBULENCE SCALE IN SUBSONIC FLOW SEPARATION

J. Leith Potter, Co-Principal Investigator
W. R. Seebaugh, Co-Principal Investigator
Carl E. Fisher, Graduate Student
R. Joel Barnett, Graduate Student
Rajiv B. Gokhale, Graduate Student

Sponsored Research Project RG-5997
NASA Research Grant NAG-1-483

Interim Progress Report 2

Period Covered: 1 January 1985 - 30 June 1985

TABLE OF CONTENTS

	Page
List of Tables	iii
List of Illustrations	iv
Nomenclature	vi
Introduction	1
Experimental Equipment and Methods	1
Equipment Description	1
Wind-Tunnel Flow Instrumentation	3
Signal Analysis	4
Airfoil Model Instrumentation	6
Turbulence Parameters	7
Intergal Scale	7
Dissipation Scale	8
Turbulence Intensity	9
Power Spectrum	9
Experimental Results	10
Wind-Tunnel Flow	10
Airfoil Model	14
Project Status and Plans	16
References	17
Tables	18
Illustrations	21

LIST OF TABLES

Page

TABLE 1: TURBULENCE INTENSITY, INTEGRAL SCALE, AND DISSIPATION LENGTH IN 41-CM TEST SECTION..... 18

TABLE 2: TURBULENCE INTENSITY, INTEGRAL SCALE AND DISSIPATION LENGTH IN 102-CM TEST SECTION..... 19

TABLE 3: EFFECT OF 6.18:1 CONTRACTION ON INTEGRAL SCALE..... 20

LIST OF ILLUSTRATIONS

		Page
1.	Vanderbilt Subsonic Wind Tunnel	21
2a.	Turbulence Grid #3	22
2b.	Turbulence Grid #4	23
3a.	Airfoil Model Installed in 41-cm Test Section	24
3b.	Hot-Film Boundary-Layer Probe	25
4.	Instrumentation Connection	26
5.	Turbulence Parameters in 41-cm Test Section	27
6.	Turbulence Parameters in 102-cm Test Section	28
7.	Integral Scale in 41-cm Test Section (10.16-cm Grid)	29
8.	Integral Scale in 41-cm Test Section (5.08-cm Grid)	30
9.	Integral Scale in 102-cm Test Section (10.16-cm Grid)	31
10.	Integral Scale in 102-cm Test Section (5.08-cm Grid)	32
11.	Power Spectrum for 5.08-cm Grid at 234.5 cm	33
12.	Autocorrelation for 5.08-cm Grid at 234.5 cm	34
13.	Autocorrelation Function at Position 173.2 cm	35
14.	Power Spectrum at Position 173.2 cm	36
15.	Autocorrelation Function at Position 265.7 cm	37
16.	Power Spectrum at Position 265.7 cm	38
17.	Autocorrelation Function with no Grid	39
18.	Power Spectrum with no Grid	40
19.	Integral Scale as a Function of X/M	41
20.	Dissipation Length Parameter in 41-cm Test Section (10.16-cm Grid)	42
21.	Dissipation Length Parameter in 41-cm Test Section (5.08-cm Grid)	43
22.	Dissipation Length Parameter in 102-cm Test Section (10.16-cm Grid)	44
23.	Dissipation Length Parameter in 102-cm Test Section (5.08-cm Grid)	45

Page

24. Spoiler and Surface Film Pattern..... 46

25. Upper Surface Pressure Coefficient..... 47

26. Boundary Layer Velocity Profile..... 48

NOMENCLATURE

Symbols	Definition
b	Grid bar width or diameter
f	Longitudinal correlation coefficient
J	Eulerian time scale
L_d	Dissipation Length Parameter
L_x	Longitudinal Integral Scale
M	Grid element mesh size
p_a	Atmospheric pressure
p_o	Stagnation pressure
p^*	Local pressure
p	Static pressure
Q	Correlation between velocity components in space
R	Correlation Coefficient
R_b	Reynolds number, Ub/ν
T	Turbulence intensity
t	Time
t'	Autocorrelation time step
U	Velocity
u,v	Cartesian fluctuating velocity components in the x and y directions, respectively
x	Cartesian spatial coordinate
x_o	Integral scale virtual origin

Symbols	Definition
λ_f	Longitudinal dissipation length scale
ν	Kinematic viscosity, μ/ρ
μ	Dynamic viscosity
ρ	Density
Subscripts	
A,B	Between the points A and B in space
i,j	In the i and j directions in space
o	Initial, or at the origin
u	Velocity correlation
x	Spatial correlation
Operators	
$\overline{Z}$	Average Value of Z
Z'	Root-mean-square value of Z

INTRODUCTION

This is a report of progress during the period from 1 January to 30 June, 1985, the second half of the initial grant period (1 July, 1984 to 30 June, 1985). Earlier progress for this grant period is reported in Reference 1. The grant was recently extended through 30 June, 1986.

The objective of this work is the clarification of the role of freestream turbulence scale in determining the location of boundary layer separation. Considerable progress toward this objective was made during the current reporting period. All contemplated modifications to the test facility have been completed. Wind tunnel flow characteristics, including turbulence parameters, have been determined with two turbulence-generating grids, as well as with no grid. These results are summarized herein and major parts of the research are described in detail in two theses (Refs. 2 and 3). Initial results on the role of scale on turbulent boundary-layer separation on the upper surface of an airfoil model are also discussed in this report. Further work on laminar, transitional, and turbulent separation on the test model will be discussed in subsequent progress reports.

EXPERIMENTAL EQUIPMENT AND METHODS

Equipment Description

The Vanderbilt University Engineering School Wind Tunnel is described in Reference 1. The wind tunnel has been modified recently by adding a large multi-vaned exit diffuser (Figure 1). The diffuser is used to break up the exhaust air jet and produce a more uniform return flow to the wind tunnel entrance. The diffuser reduces the upstream propagation of disturbances from the tunnel exit which affect measurements of intensity and scale in the small (41 cm) test section. All data in this report were obtained with the diffuser installed.

Wind tunnel flow characteristics have been determined for two turbulence-producing grids, as well as with no grid, with both test sections empty. These grids, of square mesh construction, have the following characteristics:

Grid #1: 1.27 cm x 1.90 cm bars with 10.16 cm mesh spacing
(1.27 cm side normal to flow direction)
(M/b = 8.00)

Grid #2: 0.32 cm-dia. rope with 5.08 cm mesh spacing
(M/b = 16.00)

These grids were constructed to mount on four rails located along the inner walls of the large (102-cm) test section. They can be located at any desired longitudinal station. Photographs of grid #1 are shown in Reference 1. Both grids are constructed to facilitate insertation and removal through the access panels on the sides of the test section, and fit snugly against the walls of the test section to reduce leakage.

Two additional grids were constructed following the initial airfoil tests. Wind tunnel flow characteristics with empty test sections are not yet available for these grids. The construction details of these grids are:

Grid #3: (Modification of Grid #1):
1.27 cm x 1.90 cm bars with 5.08 cm mesh spacing
(1.27 cm side normal to flow direction)
(M/b = 4.00)

Grid #4: 0.64 cm-dia. bars with 2.54 cm mesh spacing
(M/b = 4.00)

Grid #3, shown in Figure 2a, also mounts in the 102-cm test section. Grid #4 (Figure 2b) was designed to be mounted at the entrance to the 41-cm test section, following the contraction (Figure 1).

The principal test model for this research is a modified NACA 0015

airfoil with a chord length of 40 cm. Only the upper surface of the airfoil has the standard NACA countour. The lower surface was made flat (tangent to the circular-arc leading edge) to reduce flow blockage. The model, which is constructed of Plexiglas, is shown installed in the 41-cm test section in Figure 3a. Also shown is a hot-film boundary-layer probe and the associated drive mechanism. The probe itself is shown in Figure 3b.

Wind-Tunnel Flow Instrumentation

Velocity measurements for turbulence intensity and integral scale (see following section for definitions) were made with a Thermo-Systems Inc., Model 1010 hot-wire anemometer operating in the constant-temperature mode with an overheat ratio of 1.65. The hot-wire probe used was a TSI Model 1210-T1.5 hot-wire probe made from platinum plated tungsten wire 0.004-mm in diameter and 1.25-mm long. A TSI Model 1076 True RMS digital voltmeter was used for independent measurements of wind tunnel mean velocity and turbulence intensity. The DC output function of the meter was also used in calibrating the output voltage of the anemometer to the tunnel mean velocity.

The hot-wire anemometer must be re-calibrated whenever the probe wire is replaced or when there are significant changes in the range of speeds for which calibration has been performed. One example of the latter case occurs when there is movement of the probe from the high-speed test section to the low-speed section. Calibration is also performed whenever the output from the anemometer appears to deviate substantially from previous data at the same mean velocity.

Calibration of the hot-wire anemometer is performed by comparison of the anemometer output voltage to the free-stream velocity. The latter is indicated by a high accuracy MKS-Baratron differential pressure transducer connected to

a calibrated static pressure port located in the wind tunnel's 41-cm test section and referenced to atmospheric pressure. The test section static pressure port is calibrated with a pitot-static tube so that the differential pressure measurement ($p_a - p^*$) is proportional to the dynamic pressure measured by the pitot-static tube, viz.

$$(1/2)\,\rho U^2 = p_o - p_\infty = C \cdot (p_a - p^*) \qquad (1)$$

The output of the differential pressure sensor (volts) is displayed by a high precision DC voltmeter, where the output voltage is related to the differential pressure (mm Hg) by

$$9.9981 \cdot (\text{voltage indicated}) = p_a - p^* \qquad (2)$$

After the tunnel mean velocity is calculated from the above relations, calibration parameters for the hot wire anemometer are found using a least-squares power function fit of the form

$$U = A \cdot (\text{Anemometer voltage})^B \qquad (3)$$

rather than using a signal linearizer as is frequently done. This allows for a much less tedious correction of the signal when re-calibration is needed. It also prevents distortion of auto-correlation results due to changes in the required linearizer coefficients. Velocity error for any point by using this method was typically less than 0.5 percent in the velocity range of interest and less than 2.0 percent at the velocity extremes.

Signal Analysis

Analysis of the anemometer output centers on the fluctuating component of the instantaneous velocity. Measurements of turbulence intensity and of turbulence integral length scale are found by routing the anemometer signal through an active 12 dB/octave high-pass filter with a cutoff frequency of 100 Hz to bias out both the DC or mean-velocity component and the fluctuating velocity components below approximately 10 Hz. The 100 Hz cutoff was selected because

(1): it was apparent that there was a significant 60 Hz component contributed by the lighting and equipment in the Fluid Dynamics Research Laboratory, and (2): it was argued that the fluctuations at frequencies less than the cutoff were not true turbulence, but rather "flow unsteadiness". This follows from consideration of mean flow speed and dimensions of the wind tunnel, as done in Reference 4. Spectral analysis of the anemometer output with a Bruel & Kjaer Model 2033 Real-Time Spectrum Analyzer showed extremely high intensity in this region (80 dB at 10 Hz relative to 60 dB at 100 Hz). The 100 Hz high pass filter reduced the 60 Hz component by 12 dB and the lower frequency components by at least 30 dB.

After passing through the high-pass filter, the signal was digitized by a Interactive MicroWare Inc., 12-bit Analog-Digital converter which sampled the analog signal at 13.5 kHz under the direction of an APPLE IIe micro-computer. The input range of the A/D converter was set for ± 100 mv which gave a resolution of 0.0488 mv/bit. This method of biasing out the steady component and using the most sensitive range available on the A/D system improves the autocorrelation accuracy. With the DC component included, the resolution of the system is 1.22 mv/bit.

The length of signal recorded in this manner was 10,000 points, for a time interval of 0.74 sec. An average value for the DC anemometer output voltage was determined using a Thermo-Systems Inc. voltmeter operating in the DC mode. This measurement was made just prior to recording the fluctuating voltage using the APPLE IIe computer and the A/D converter. Along with the anemometer signal, 384 readings of the differential pressure transducer output voltage were averaged over 1 sec to be used to calculate the tunnel mean velocity. The data, as written to the APPLE IIe diskettes for later transfer to the Vanderbilt mainframe computer, were in the form

Number of anemometer data readings
A/D converter gain setting
A/D converter sampling period (microseconds)
Averaged MKS transducer reading (V)
Averaged DC component of anemometer output (mV)
String of anemometer data

The unprocessed data from the APPLE computer were next transferred to the Vanderbilt University main-frame Digital Equipment Corp., DEC-1099 computer using the micro-to-main-frame file transfer program KERMIT available to on-campus users. On the DEC-1099, the data were processed to calculate the turbulence intensity, integral scale, and dissipation length parameter. Spectral analysis of the data using the Fast-Fourier-Transform was also accomplished on the DEC-1099. Figure 4 shows a schematic diagram for the collection and analysis of the data.

Airfoil Model Instrumentation

Velocity measurements within and just above the boundary layer on the upper surface of the airfoil model are made with a TSI Model 1218-20W hot-film probe (Figure 3). This probe is positioned by a hand-operated micrometer screw attached to the upper wall of the wind tunnel. The equipment described in the previous section is used to obtain and reduce data obtained using this probe.

Static pressure orifices are installed in the upper surface of the airfoil model at the leading edge and at intervals of approximately 1.25 cm in the downstream direction. The orifices are connected by plastic tubing to the inlet ports of a 24-position Scanivalve Model DSS 24C scanner. All pressures are read on a single high-accuracy MKS-Baratron pressure transducer, using local atmospheric pressure as a reference. The transducer output is displayed by a high precision DC voltmeter. The relationship between differential pressure and voltage is similar to that given by Equation (2).

TURBULENCE PARAMETERS

The parameters used to describe the wind tunnel flow are discussed in Reference 1. The definitions of the parameters for which results are included herein are repeated for convenience.

Integral Scale

The integral scale reflects the correlation or connection between fluctuating velocity components in a flow field. This correlation can be between two different points in the flow field or it can be a correlation between the velocities at the same point at different times. The spatial correlation is generally called the cross-correlation and the temporal correlation is the auto-correlation.

In homogeneous isotropic flow, the correlation between the fluctuating velocity components u_a and u_b at two different points A and B is defined as

$$Q_{A,B} = \overline{(u_a)_A (u_b)_B} \tag{4}$$

since the relationship between the velocity fluctuations is independent of the choice of a coordinate system. Typically the cross-correlation coefficient

$$R_{A,B} = \overline{(u_a)_A (u_b)_B} / (u_a')_A (u_b')_B \tag{5}$$

is used instead of the cross-correlation.

One can similarly state the expression for the auto- or Eulerian correlation. Here the correlation between the fluctuation velocity at a fixed point at two different times t) and (t + t) is of interest. The correlation is then

$$\overline{u(t)u(t + t')} \tag{6}$$

and the auto-correlation coefficient is

$$R_u(t') = \overline{u(t)u(t + t')}/u'^2 \tag{7}$$

where u'^2 is the mean square fluctuation and the average is taken with respect to the time step t'.

In a homogeneous flow field with a constant mean velocity which is large compared to the fluctuating components, one can make use of Taylor's approximation,

$$\partial/\partial t = -\overline{U}(\partial/\partial_x) \tag{8}$$

to get the relationship between the longitudinal cross-correlation coefficient, f, and the auto-correlation coefficient, $R_u(t')$

$$f(x) = R_u(t') \tag{9}$$

Here the reference is a stationary observer watching the turbulent flow field moving past at the mean velocity U, with small velocity fluctuations, u.

The Eulerian time scale of the turbulence fluctuations,

$$J_u = \int_0^\infty R_u(t')dt' \tag{10}$$

is a time-domain measure of the longest connection between the turbulent fluctuations in the flow direction. Just as was done for the relationship between the cross- and auto-correlations, the integral scale of turbulence, a spatial measure of the average size of the turbulent eddies, is

$$L_x = \overline{U}J_u \tag{11}$$

Dissipation Scale

The dissipation length scale is a measure of the size of the turbulent eddies responsible for the dissipation of energy through viscous stresses. By using a spatial correlation procedure on the longitudinal velocity fluctuations in a homogeneous turbulent flow field one can find (Ref. 5)

$$f(x) = 1 - (x^2/\lambda_f^2) \tag{12}$$

which defines the micro- or dissipation scale

$$1/\lambda_f^2 = 1/2u'^2\,[\partial u/\partial x]^2\,|_{x=0} \tag{13}$$

The above equation for f(x) defines a parabola with its vertex at (x,f) = (0,1). The dissipation length scale may also be found from the intersection of this curve with the x-axis.

Another method of characterizing the size of the smallest eddies present in a grid-induced turbulent flow field is to use the dissipation length parameter, L_d. In homogeneous isotropic turbulence the equation for turbulence energy can be written (Ref. 6),

$$U(du^2/dx) = -10\ \nu\ u^2/L_d^2 \tag{14}$$

By measuring the decay of the turbulence intensity downstream of a turbulence-inducing grid, one can use the above equation to calculate the dissipation length parameter. In this report the dissipation length parameter is used as a measure of the size of the dissipative eddies, rather than the dissipation length scale.

Turbulence Intensity

Scale is only part of the information needed in studying turbulence. It is also important to know the relative violence or intensity of the turbulent fluctuations about the mean flow velocity. Intensity is generally defined in turbulence as

$$u' = \sqrt{u^2} \tag{15}$$

and the relative intensity is generally

$$T' = u'/\overline{U} \tag{16}$$

By measuring the root-mean square of the fluctuating component of the velocity and the mean component, the turbulence intensity may be calculated from the above relation.

Power Spectrum

One can develop a frequency distribution for the kinetic energy of the various-sized eddies. Spectral analysis of the fluctuating velocity components is accomplished through the Fast Fourier Transform of the hot-wire anemometer output voltage. The power spectrum produced can be used to determine the wavelengths of the primary energy-containing eddies.

EXPERIMENTAL RESULTS

Wind Tunnel Flow

Table 1 presents results of turbulence intensity, integral scale, and dissipation-length parameter measurements for both the 5.08-cm-mesh grid and the 10.16-cm-mesh grid in the 41-cm test section. Table 2 presents these parameters for both grids in the 102-cm test section. Figures 5 and 6 are parameter maps produced from these two tables to outline the range of conditions covered.

Integral Scale: The integral scales produced by the 10.16-cm-mesh grid and the 5.08-cm-mesh grid in the 41-cm test section and the 102-cm test section are shown versus the distance from the grid to the probe, x, in Figures 7, 8, 9, and 10 respectively. In each case, a virtual origin represented by x_0 was selected to produce an equation for the integral scale of the form (see Naudascher and Farrell, Ref. 6):

$$L_x = a(x - x_0)^b \tag{19}$$

The virtual origin, at station x_0, was selected to produce the best fit to the data using a non-linear optimization technique. For the 41-cm test section the data from the 10.16-cm-mesh grid give a virtual origin far upstream of the grid (20 to 800 cm), while data for the 5.08-cm-mesh grid give a virtual origin that varies from 800-cm upstream of the grid to 130-cm downstream of the grid. This variation is a consequence of the scatter of the integral scale data and the use of a fitting technique which treats all data points equally. A technique based on judgment and expected similarity for the grid at the three speeds leads to the single curve shown as a broken line in Figure 8 and an alternate curve for the top speed in Figure 9.

Meier and Kreplin (Ref. 7) have shown how small changes in the frequency spectrum of the velocity signal can influence the integral scale obtained by the autocorrelation method. Spectral analysis of the data collected for the

5.08-cm-mesh grid at x = 234.5 cm (Figure 11) shows definite peaks which cause additional peaks in the autocorrelation function (Figure 12), leading to an increase in the integral scale as compared to the smoothed autocorrelation also shown.

Integral scale variation due to a non-smooth frequency spectrum is more typical of the 5.08-cm-mesh grid than of the 10.16-cm-mesh grid. A comparison of the autocorrelation functions and power spectra for both grids, with the probe located in the 41-cm test section and at grid positions 173.2 cm and 265.7 cm, shows that in all cases the 10.16-cm-mesh grid produces smoother results (Figures 13-16). This may be related to the generally higher turbulence intensity associated with that grid. Regular peaks in the autocorrelation function also appear with no grid installed in the wind tunnel. Figures 17 and 18 show these peaks in the autocorrelation function and in the power spectrum, respectively, at a mean velocity of 50.6 m/s. It is apparent from these results that there was a decrease of the integral scale as the grid mesh decreased. Figure 19 shows the change in the integral scale at 50.6 m/s as x/M varies for the 5.08-cm and 10.16 cm grids, and for no grid. When no grid is used, the integral scale is largely determined by the 6.3-mesh/cm screens through which the flow passes after entering the tunnel and going through the honeycomb flow straighteners which have cells of 9.5 mm x 8 mm. This case then represents very large x/M and is not shown in Figure 19.

In the 102-cm test section the integral scale also increases as distance from the grid increases (Figs. 9,10). Here also, the virtual origin calculated by the power law curve fit is always upstream of the 10.16-cm-mesh grid and downstream of the 5.08-cm-mesh grid. The integral scale variation over the range of grid positions used was ± 10 percent for the 10.16-cm-mesh grid and ± 15 percent for the 5.08-cm-mesh grid at a mean velocity of 3.65 m/s. At

71.3 m/s the variation was ± 12 percent for the 10.16-cm-mesh grid and ± 50 percent for the 5.08-cm-mesh grid over the same range of grid positions.

Table 3 indicates the effect of the 6.18:1 contraction on the integral scale produced by both the 10.16-cm-mesh grid and the 5.08-cm-mesh grid mounted in the 102-cm test section. With each grid, the contraction causes a significant increase of the integral scale, with the effect being more pronounced with the 5.08-cm-mesh grid. These results agree fairly well with those of Tan-atichat et al.(Ref. 8) who measured the change in integral scale produced by a 7.64:1 area-ratio contraction downstream of a 2.54-cm-mesh grid with an inlet free-stream velocity of 4.9 m/s. The downstream integral scale was approximately 2.5 times that of the inlet integral scale; however, their results also show a further decrease in the integral scale as the distance from the contraction exit increased. They assert that the integral scale should decrease with distance downstream of the contraction if there are no further disturbances in the tunnel. It is not possible to verify this statement here because the disturbances produced by the wind tunnel blower have been found to propagate upstream and impose a secondary source of turbulence which competes with the grid-produced turbulence (Ref. 3). It is suggested that this competition between the two sources has existed in many of the investigations reported in the literature on grid-induced turbulence (Ref. 9). The integral scales presented here, and their variations, were no doubt affected by this.

In addition, Tan-atichat et al.(Ref. 8) indicate that the degree to which the contraction increases the integral scale is affected by the character of the inlet flow turbulence. If the turbulence is small in scale, then the contraction has less effect than if the incoming turbulence is large in scale. This could account for the difference in the contraction effect between these two studies. Here, the inlet scale is always small so that the contraction has only a moderate effect, rather than the 5 to 15 magnification produced by Tan-atichat et al.

Dissipation Length: As mentioned above, the dissipation length is used as a measure of the size of the smallest turbulent eddies, these eddies being responsible for the conversion of energy through viscous dissipation. Castro (Ref. 10) gives an expression for the dissipation length parameter, L_d, as

$$\frac{L_d}{M} = \eta\left(\frac{1}{C}\right)^{1/2n}\left[\frac{x - x_o}{M}\right]^{1-1/2n} \tag{20}$$

where the virtual origin, x_o, is determined by projecting the best-fit line for the turbulent energy decay u'^2/U^2 to zero and n is found by fitting the data with a curve of the form

$$\left[\frac{u'^2}{U^2}\right]^{-n} = C \cdot \frac{x - x_o}{M} \tag{20a}$$

In connection with this research work, Gokhale (Ref. 3)* calculated the dissipation length parameter using the turbulence intensity produced by both the 5.08-cm-mesh grid and the 10.16-cm-mesh grid in the 41-cm test section and the 102-cm test section. The results are presented here in Figures 20-23.

Integral Scale vs. Dissipation Length. In an attempt to present a unified theory for the analysis of grid-induced turbulence, Naudascher and Farell (Ref. 6) have developed a relationship between the macro-scale and the micro-scale of the turbulent flow field behind a grid. This relationship between the integral scale, L_x, and the dissipation length parameter, L_d, is

$$L_x/b = (L_{x\infty} - L_{xo})(L_d/b)/L_{d\infty} + L_{xo}/b \tag{21}$$

Using the constants L_{xo}, $L_{x\infty}$, and $L_{d\infty}$ as given, agreement between the actual results and the equation given above was fair for the 5.08-cm-mesh grid and

*See Gokhale (Ref. 3) for a complete review of dissipation length parameters measured in the Vanderbilt subsonic wind tunnel.

rather poor for the 10.16-cm-mesh grid. This may have been due to the same virtual origin being used in Eq. (21) for the integral scale and the dissipation length parameter. The present experimental data do not support the single or common virtual origin.

The results of Bradshaw (Ref. 11) also indicate that downstream of a biplanar grid $L_d = 4.5\ L_x$. There was reasonable agreement with this result from both the 5.08-cm-mesh grid ($2.16 < L_d/L_x < 4.32$) and the 10.16-cm-mesh grid ($2.82 < L_d/L_x < 6.56$) in the 102-cm test section. However, the effect of the contraction is to increase the integral scale and decrease the dissipation length, giving completely different results in the 41-cm test section. In the 41-cm test section $\overline{L_d/L_x} = 0.60$ for the 10.15-cm-mesh grid and $\overline{L_d/L_x} = 0.40$ for the 5.08-cm-mesh grid. For more details see Gokhale (Ref. 3).

Airfoil Model

Three types of data have been acquired using the airfoil model in the 41 cm test section: (1) flow visualization, (2) surface pressure, and (3) boundary layer survey. Example results are included herein; complete data will be described in detail in subsequent progress reports.

Flow Visualization: As discussed in Ref. 1, flow visualization methods are very important in determining the location of separation on the airfoil model. In fact, the first results with the airfoil model indicated that a desirable separation pattern could not be obtained at any angle of attack. Separation did not occur at the lower angles. At the higher angles where separation did occur, the chordwise location of the separation varied across the span and large vortices were apparent over the outboard portions of the airfoil surface. Similar patterns have been photographed by other researchers.

In order to obtain an approximately straight (spanwise) separation line, flaps and spoilers of various configurations were installed on the upper surface

of the airfoil model near the trailing edge. A satisfactory flow pattern was obtained with a spoiler of rectangular cross section (1.9 cm high x .88 cm thick) located across the upper surface with its leading edge at the 86 percent chord line. The spoiler and the associated surface flow pattern (obtained using the liquid film mixture given in Ref. 1) are illustrated in Figure 24 for an angle of attack of 5 degrees. One of the end plates used to attach the spoiler to the airfoil model is also shown in the figure.

The upper surface pressure coefficient obtained with the spoiler installed is shown in Figure 25 for the 5-degree angle of attack. Grid #1 was installed when this pressure distribution was obtained. Separation occurred at a chordwise distance of approximately 30 cm and was very repeatable.

A number of surface pressure distributions were obtained using grid #1 and grid #2 over the range of locations given in Table 1. Data were obtained with a smooth airfoil and with a boundary layer trip installed near the leading edge. All pressure distributions with a turbulent boundary layer were very similar to that shown in Figure 25, and little or no variation was observed in the surface flow pattern.

Following these observations, grid #3 was constructed and installed in the 102 cm test section. This grid produced a turbulence intensity of 1.19 percent and an integral scale of 0.52 cm at a freestream velocity of 50.1 m/s. Total boundary layer thickness at $x/c = 0.635$ is 1.2 cm. This location is 2 cm upstream of separation. Essentially no difference in separation location resulted. To further increase the turbulence intensity, grid #4 was installed at the entrance to the 41 cm test section. The turbulence intensity was increased to 2.85 percent at an integral scale of 0.74 cm at a freestream velocity of 49.9 m/s. Again, no observable change in separation location occurred. At the present time, it appears that the variation in separation

location was less than 0.2 cm over the entire range of flow conditions (with a turbulence boundary layer over the aft region of the airfoil model).

Preliminary boundary-layer surveys have been made at a location about 2 cm upstream of the separation location obtained with the spoiler installed. A typical profile is shown in Figure 26. Since the developing boundary layer was subjected to an adverse pressure distribution for a distance of about 25 cm, the profile shape does not display the familiar 1/7-power profile characteristic of flat plates. Turbulent boundary-layer calculations are currently being performed for the experimental conditions. Predicted profile shapes for both laminar and turbulent flow will be compared with the experimental results in a subsequent progress report.

PROJECT STATUS AND PLANS

During the last quarter, the data acquisition process has become highly automated and the rate of acquisition has increased significantly. The data collection portion of the overall (two-year) program is nearly complete. Additional data will be taken at lower Reynolds numbers to determine the effect of turbulence scale and intensity on laminar and transitional separation. It is anticipated that this effort will be completed during the next two months, which is somewhat later in the program than originally planned.

The major effort during the second year will be devoted to analyzing the data in greater depth. Any additional measurements suggested by the analysis will also be performed.

REFERENCES

1. Potter, J. L., Seebaugh, W. R., Barnett, R. J., and Gokhale, R. B., "The Role of Freestream Turbulence Scale in Subsonic Flow Separation". Interim Progress Report No. 1, NASA Grant NAG-1-483, December, 1984.

2. Fisher, C. E., "Autocorrelation and the Integral Scale in Grid Induced Turbulent Flow". Thesis, Department of Mechanical and Materials Engineering, Vanderbilt University, 1985.

3. Gokhale, R., "An Investigation of Dissipation Length Parameter of Turbulence in an Open Circuit Wind Tunnel". Thesis, Department of Mechanical Engineering, Vanderbilt University, 1985.

4. Bradshaw, Peter. An Introduction to Turbulence and its Measurement. Oxford: Pergamon Press, 1971.

5. Hinze, J. O. Turbulence, and Introduction to its Mechanisms and Theory. New York: McGraw Hill, 1959.

6. Naudascher, Eduard, and Farell, Cesar, "Unified Analysis of Grid Turbulence". Journal of the Engineering Mechanics Division, ASCE, Vol. 96, No. EM2, Proc. Paper 7214, pp. 121-141, April 1970.

7. Meier, H. U., and Kreplin, H. P., "Influence of Freestream Turbulence on Boundary-Layer Development". AIAA Journal, Vol. 18, No. 1, pp. 11-15, Jan., 1980.

8. Tan-atichat, J., Nagib, H. M., and Drubka, R. E., "Effect of Axisymmetric Contractions on Turbulence of Various Scales". Illinois Institute of Technology Report N80-32382, Sept. 1980.

9. Mueller, T. J., Pohlen, L. J., Conigliaro, P. E., and Jansen, B. J., Jr., "The Influence of Free-Stream Disturbances on Low Reynolds Number Airfoil Experiments". Experiments in Fluids, Vol. 1, No. 1, pp. 3-14, 1983.

10. Castro, I. P., "Effects of Free Stream Turbulence on Low Reynolds Number Boundary Layers". Trans. ASME, Journal of Fluids Engineering, Vol. 106, pp. 298-306, Sept. 1984.

11. Bradshaw, P., "Effect of Free-Stream Turbulence on Turbulent Shear Layers". Imperial College Aero Report 74-10, October, 1974.

TABLE 1

TURBULENCE INTENSITY, INTEGRAL SCALE, AND DISSIPATION LENGTH IN 41-CM TEST SECTION

pt No.	Turb Intensity (%)	Integral Scale (cm)	Diss Length (cm)	Grid Position (cm)	Tunnel Speed (m/s)	Grid Mesh (cm)
1	0.220	1.4347	0.3401	265.7	25.6	5.08
2	0.224	1.0922	0.3081	234.5	25.6	5.08
3	0.258	0.5860	0.2867	215.5	25.6	5.08
4	0.260	1.5109	0.3835	265.7	50.6	5.08
5	0.269	1.6233	0.3502	234.5	50.6	5.08
6	0.282	0.8408	0.2602	194.0	25.6	5.08
7	0.297	2.0213	0.3278	215.5	50.6	5.08
8	0.305	1.3821	0.5574	265.7	71.3	5.08
9	0.314	0.7808	0.3001	194.0	50.6	5.08
10	0.316	0.8129	0.4919	215.5	71.3	5.08
11	0.319	0.7274	0.2314	173.2	25.6	5.08
12	0.341	1.2613	0.5179	234.5	71.3	5.08
13	0.369	0.7133	0.4603	194.0	71.3	5.08
14	0.378	0.6965	0.2699	173.2	50.6	5.08
15	0.384	0.6346	0.1995	153.2	25.6	5.08
16	0.395	0.5337	0.4270	173.2	71.3	5.08
17	0.453	0.8240	0.6474	265.7	25.6	10.16
18	0.462	0.4520	0.2363	153.2	50.6	5.08
19	0.481	0.4268	0.3916	153.2	71.3	5.08
20	0.529	0.7024	0.5259	234.5	25.6	10.16
21	0.572	0.9825	0.8091	265.7	50.6	10.16
22	0.625	1.0904	0.8637	265.7	71.3	10.16
23	0.655	0.8601	0.6733	234.5	50.6	10.16
24	0.699	0.6379	0.4419	215.5	25.6	10.16
25	0.735	1.0623	0.7366	234.5	71.3	10.16
26	0.848	0.9431	0.6492	215.5	71.3	10.16
27	0.872	0.6367	0.3308	194.0	25.6	10.16
28	0.883	0.8129	0.5796	215.5	50.6	10.16
29	0.986	0.8286	0.4576	194.0	50.6	10.16
30	1.012	0.5683	0.1910	173.2	25.6	10.16
31	1.019	0.9212	0.5363	194.0	71.3	10.16
32	1.161	0.7189	0.3098	173.2	50.6	10.16
33	1.180	0.8626	0.4033	173.2	71.3	10.16

TABLE 2

TURBULENCE INTENSITY, INTEGRAL SCALE AND DISSIPATION LENGTH IN 102-CM TEST SECTION

pt No.	Turb Intensity (%)	Integral Scale (cm)	Diss Length (cm)	Grid Position (cm)	Tunnel Speed (m/s)	Grid Mesh (cm)
1	0.984	0.3719	1.1202	265.7	3.65	5.08
2	1.188	0.3622	0.9968	245.5	3.65	5.08
3	1.200	0.3285	0.9236	234.5	3.65	5.08
4	1.434	0.3388	0.7832	215.5	3.65	5.08
5	1.584	0.4163	1.7276	265.7	7.31	5.08
6	1.767	0.2732	0.5910	194.0	3.65	5.08
7	1.768	0.4259	1.5830	245.5	7.31	5.08
8	1.789	0.4199	1.4975	215.5	7.31	5.08
9	1.927	0.5385	2.1955	265.7	10.97	5.08
10	2.002	0.3996	1.3349	215.5	7.31	5.08
11	2.012	0.4754	2.0340	245.5	10.97	5.08
12	2.082	0.4498	1.9391	234.5	10.97	5.08
13	2.144	0.3485	1.7513	265.7	3.65	10.16
14	2.336	0.4198	1.7605	194.0	10.97	5.08
15	2.644	0.3110	1.1180	194.0	7.31	5.08
16	2.684	0.3472	1.4634	245.5	3.65	10.16
17	2.964	0.2885	1.2845	234.5	3.65	10.16
18	2.967	0.3524	1.5273	194.0	10.97	5.08
19	3.332	0.4918	2.9362	265.7	7.31	10.16
20	3.680	0.5071	3.3290	265.7	10.97	10.16
21	3.776	0.3224	0.9112	215.5	3.65	10.16
22	3.969	0.4558	2.5257	245.5	7.31	10.16
23	4.380	0.4777	2.2747	234.5	7.31	10.16
24	4.478	0.6039	2.8159	245.5	10.97	10.16
25	5.138	0.6231	2.5018	234.5	10.97	10.16
26	5.279	0.4476	1.7693	215.5	7.31	10.16
27	5.921	0.5169	1.8657	215.5	10.97	10.16

TABLE 3

EFFECT OF 6.18:1 CONTRACTION ON INTEGRAL SCALE

Grid Position (cm)	Grid Mesh (cm)	Inlet Speed (m/s)	Inlet Scale (cm)	Exit Speed (m/s)	Exit Scale (cm)	Scale Ratio (Exit/Inlet)
194.0	5.08	3.65	0.2732	25.60	0.8408	3.078
194.0	5.08	7.31	0.3110	50.60	0.7808	2.510
194.0	5.08	10.97	0.3524	71.30	0.7133	2.024
215.5	5.08	3.65	0.3388	25.60	0.5860	1.676
215.5	5.08	7.31	0.3996	50.60	2.0213	5.058
215.5	5.08	10.97	0.4198	71.30	0.8129	1.936
234.5	5.08	3.65	0.3285	25.60	1.0922	3.325
234.5	5.08	7.31	0.4199	50.60	1.6233	3.866
234.5	5.08	10.97	0.4498	71.30	1.2613	2.804
265.7	5.08	3.65	0.3719	25.60	1.4347	3.858
265.7	5.08	7.31	0.4163	50.60	1.5109	3.629
265.7	5.08	10.97	0.5385	71.30	1.3821	2.567
215.5	10.16	3.65	0.3224	25.60	0.6379	1.979
215.5	10.16	7.31	0.4476	50.60	0.8129	1.816
215.5	10.16	10.97	0.5169	71.30	0.9431	1.824
234.5	10.16	3.65	0.2885	25.60	0.7024	2.435
234.5	10.16	7.31	0.4777	50.60	0.8601	1.801
234.5	10.16	10.97	0.6231	71.30	1.0623	1.705
265.7	10.16	3.65	0.3485	25.60	0.8240	2.364
265.7	10.16	7.31	0.4918	50.60	0.9825	1.998
265.7	10.16	10.97	0.5071	71.30	1.0904	2.150

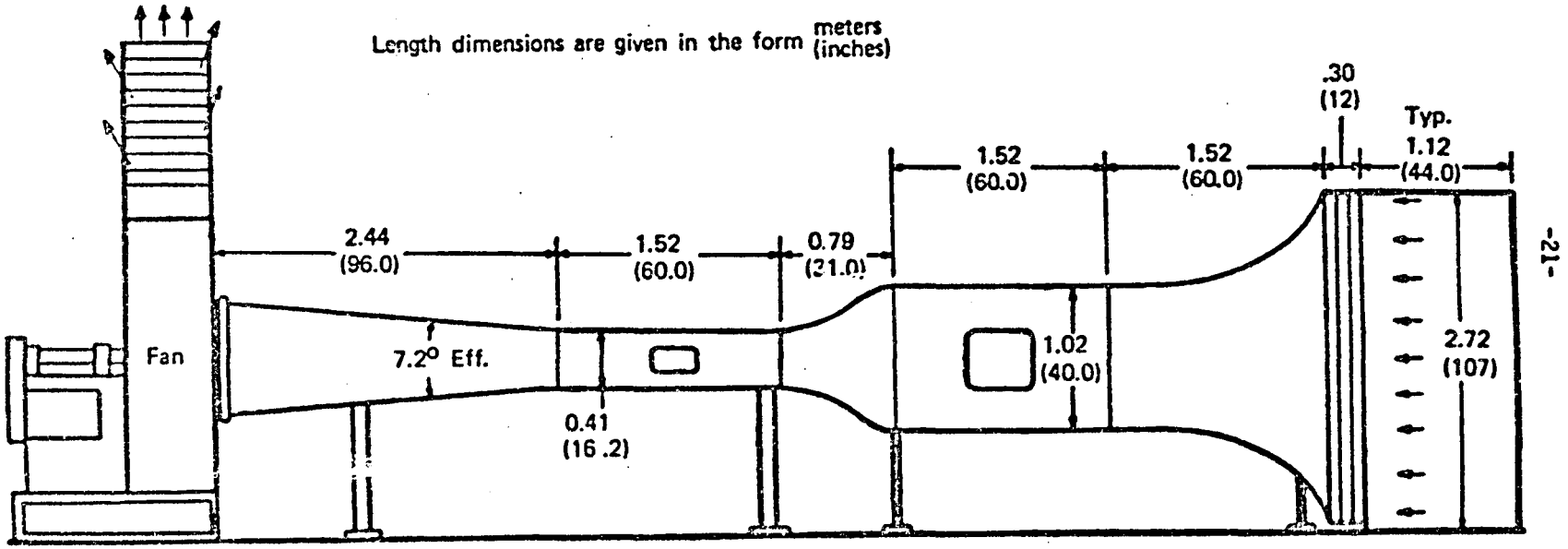

Figure 1. Vanderbilt Subsonic Wind Tunnel.

ORIGINAL PAGE IS
OF POOR QUALITY

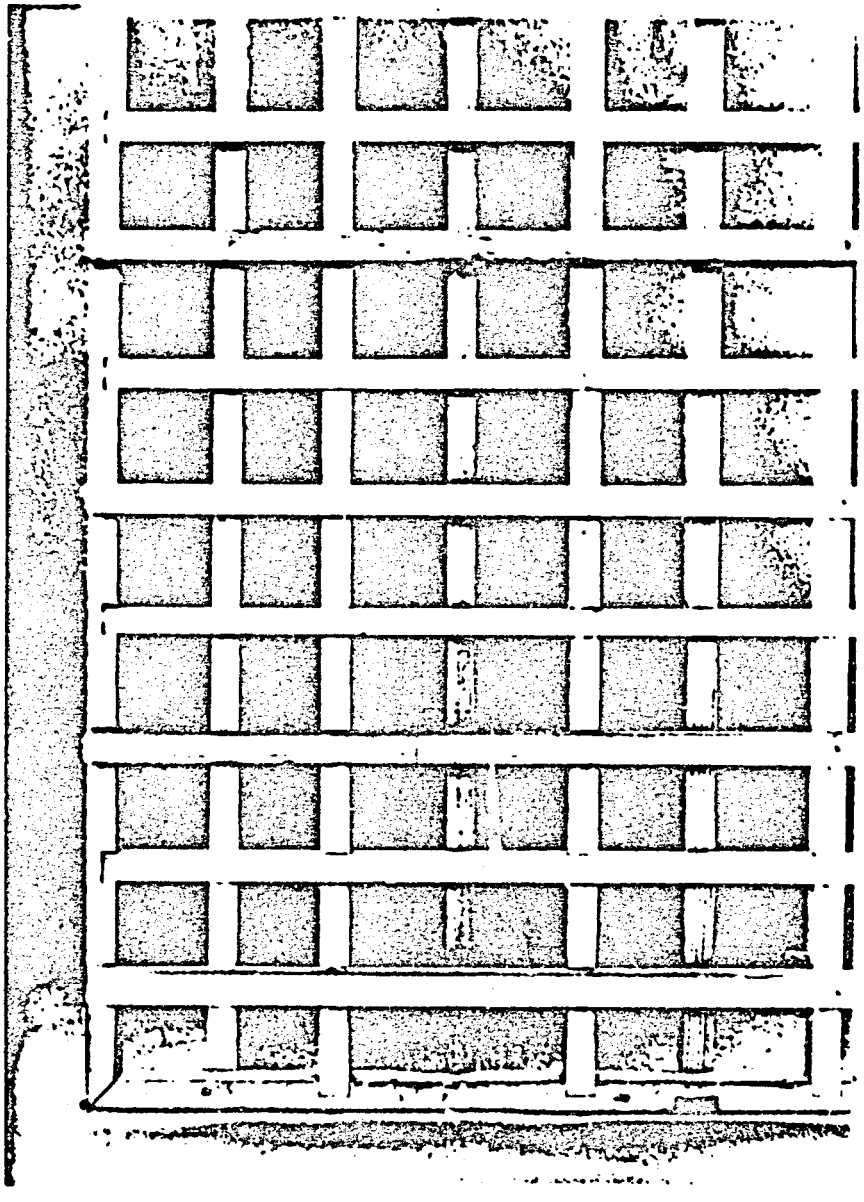

Figure 2a. Turbulence Grid #3.

ORIGINAL PAGE IS
OF POOR QUALITY

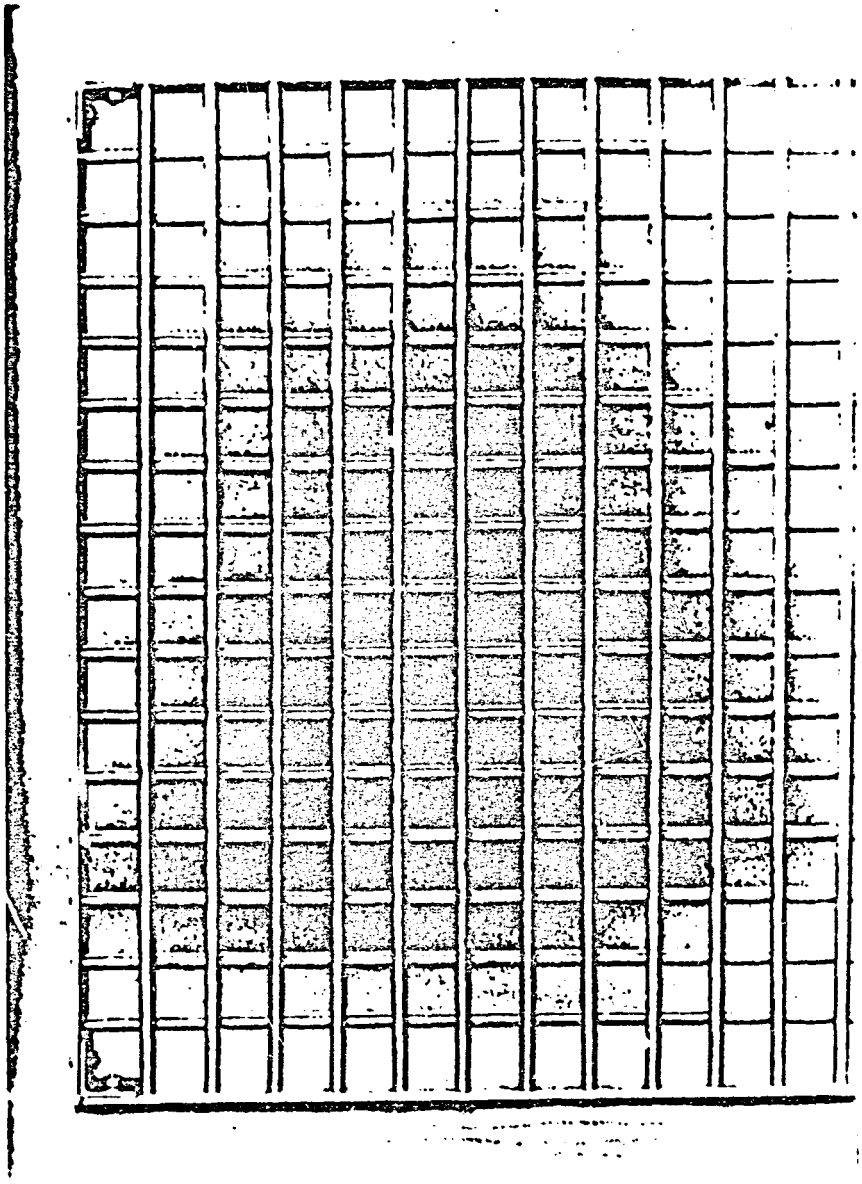

Figure 2b. Turbulence Grid #4.

ORIGINAL PAGE IS
OF POOR QUALITY

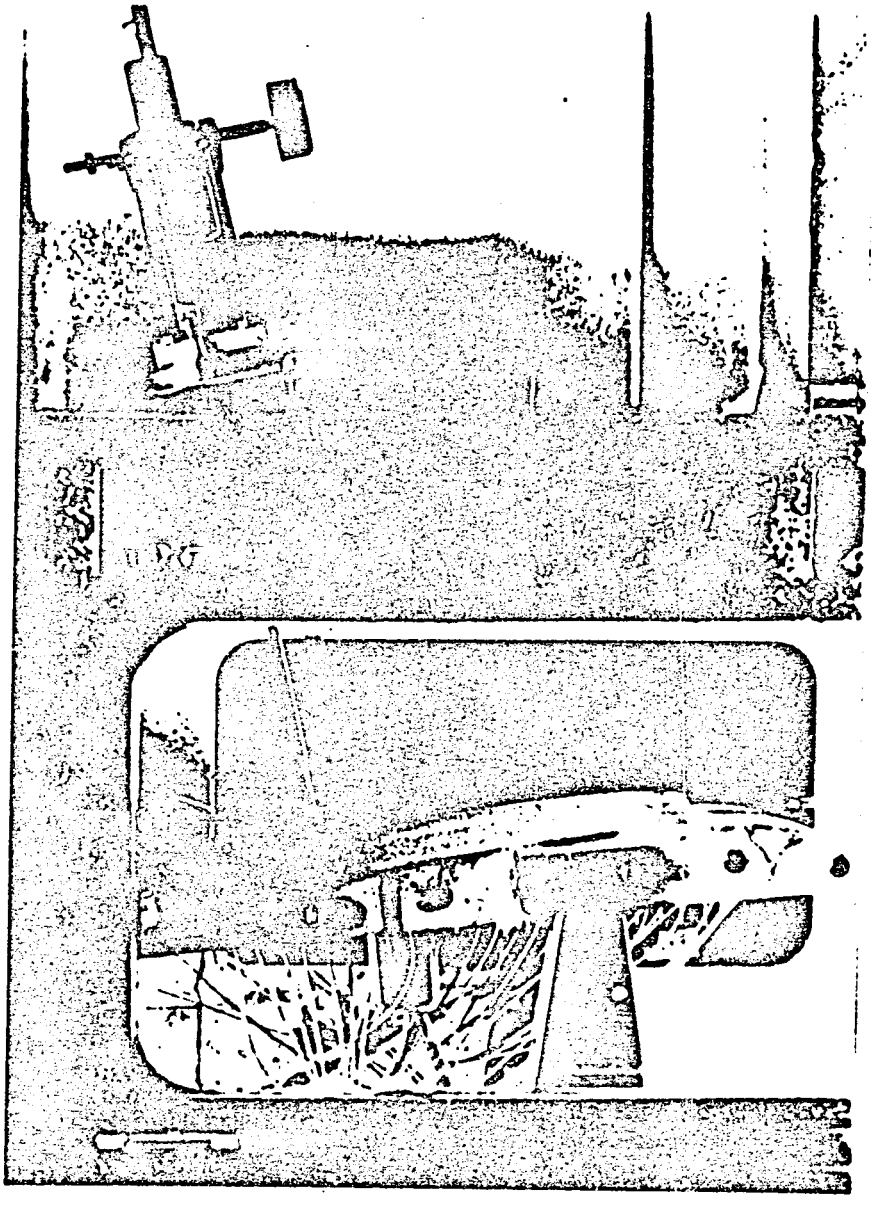

Figure 3a. Airfoil Model Installed in 41-cm Test Section.

ORIGINAL PAGE IS
OF POOR QUALITY

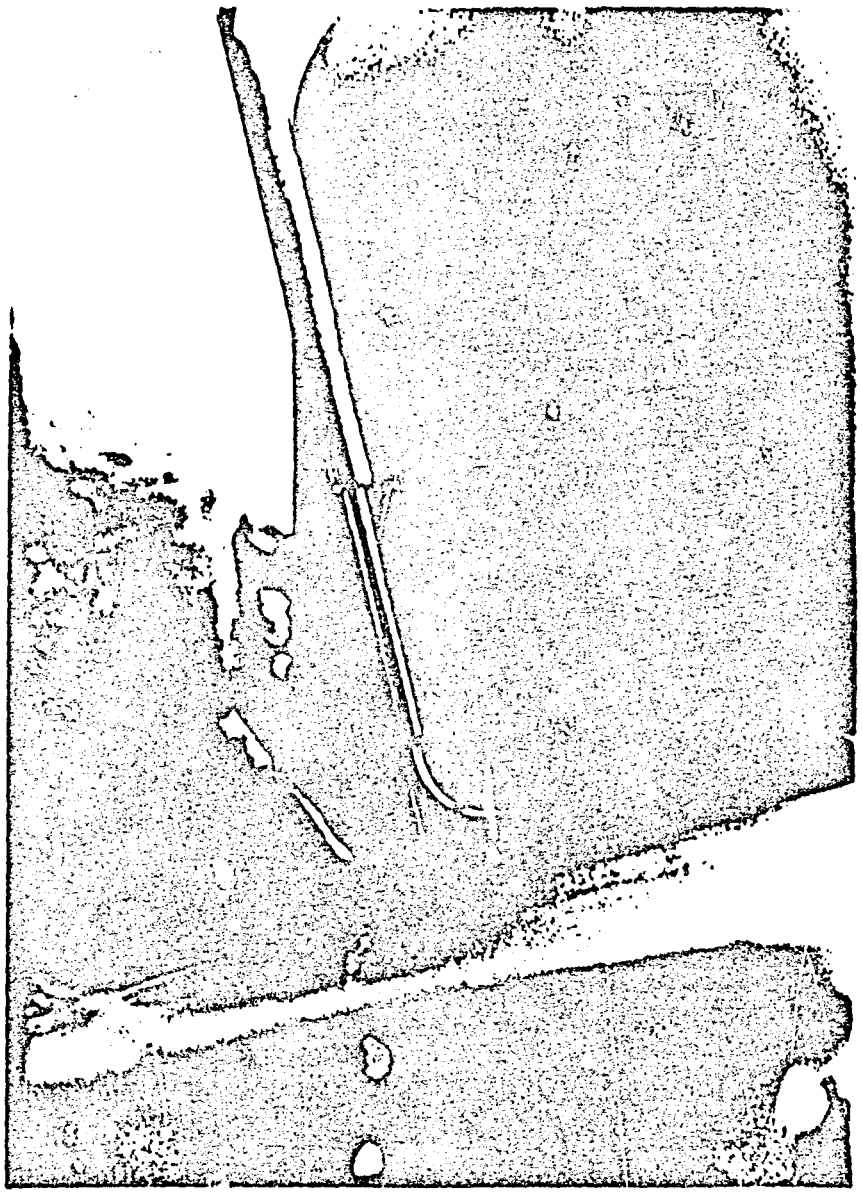

Figure 3b. Hot-Film Boundary-Layer Probe.

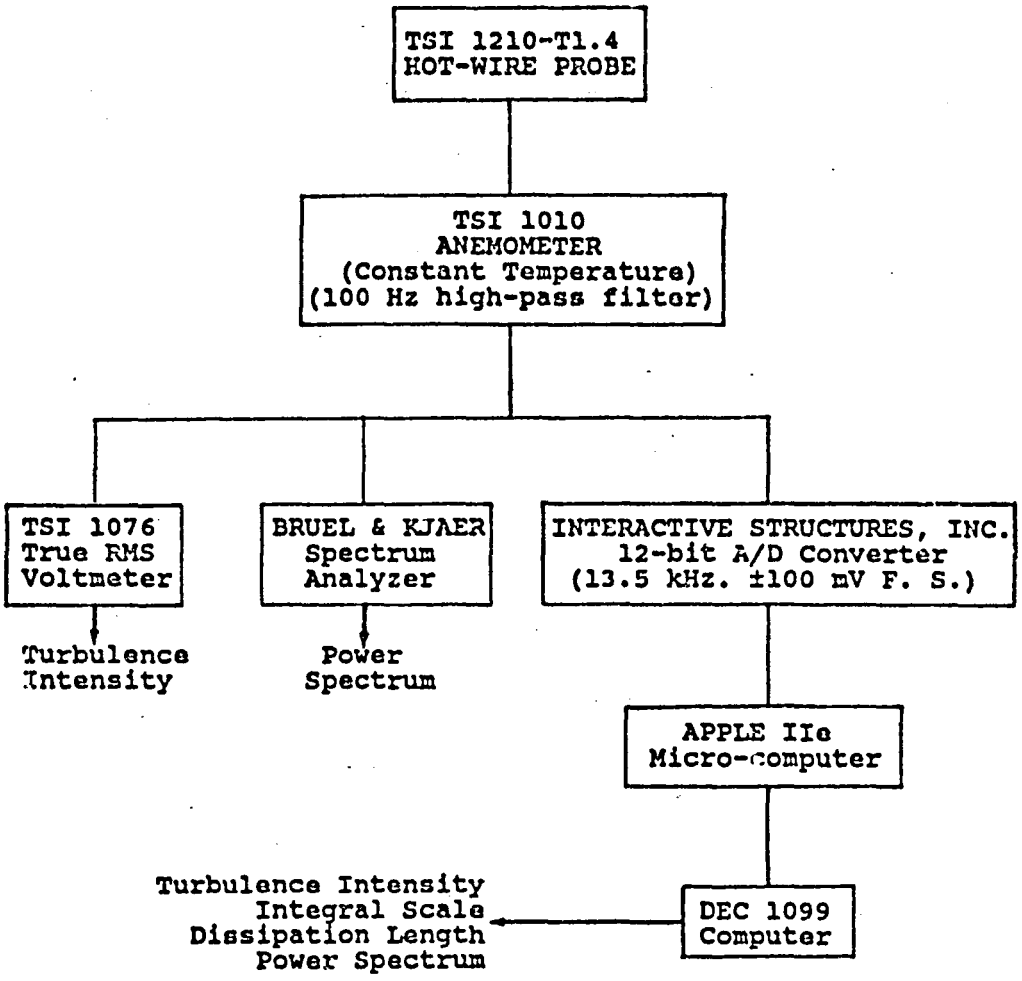

Fig. 4. Instrumentation Connection.

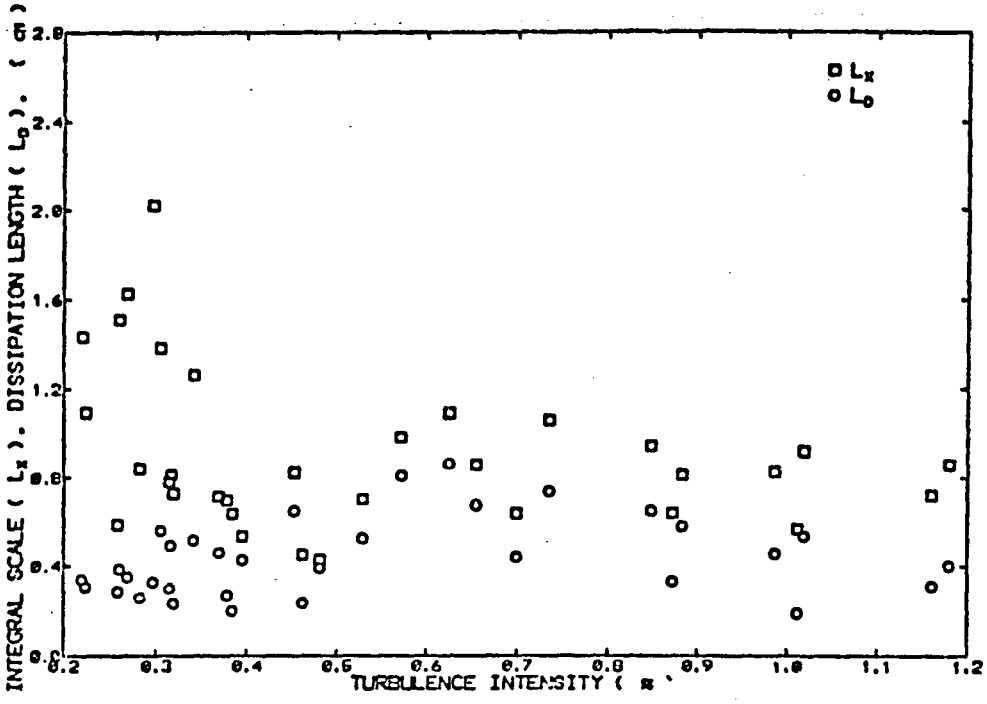

Fig. 5. Turbulence Parameters in 41-cm Test Section.

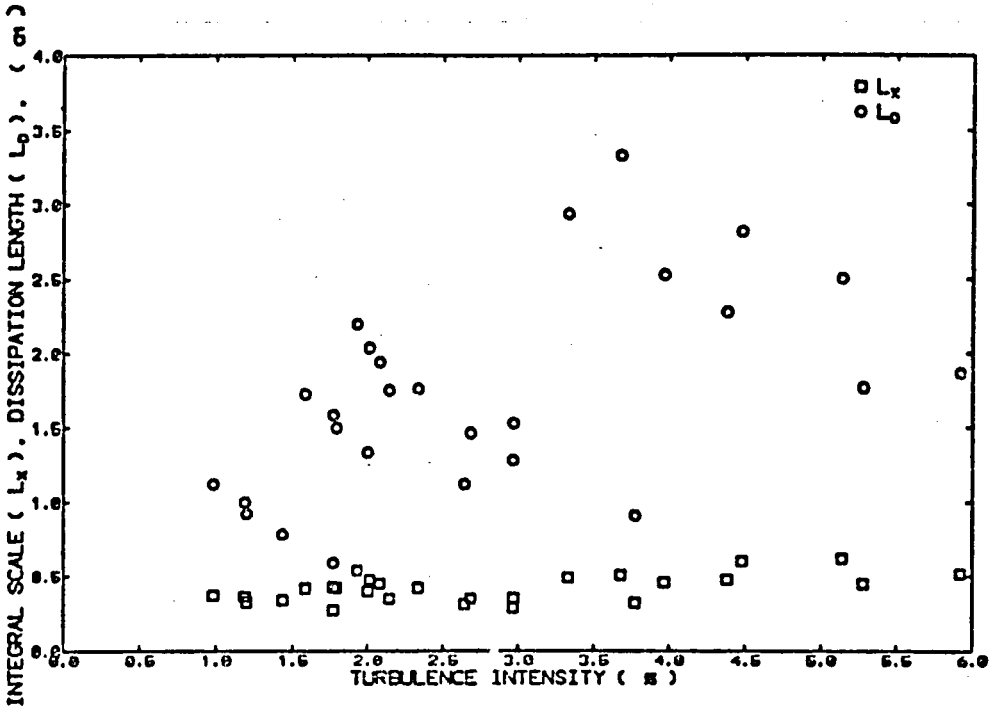

Fig. 6. Turbulence Parameters in 102-cm Test Section.

ORIGINAL PAGE IS
OF POOR QUALITY

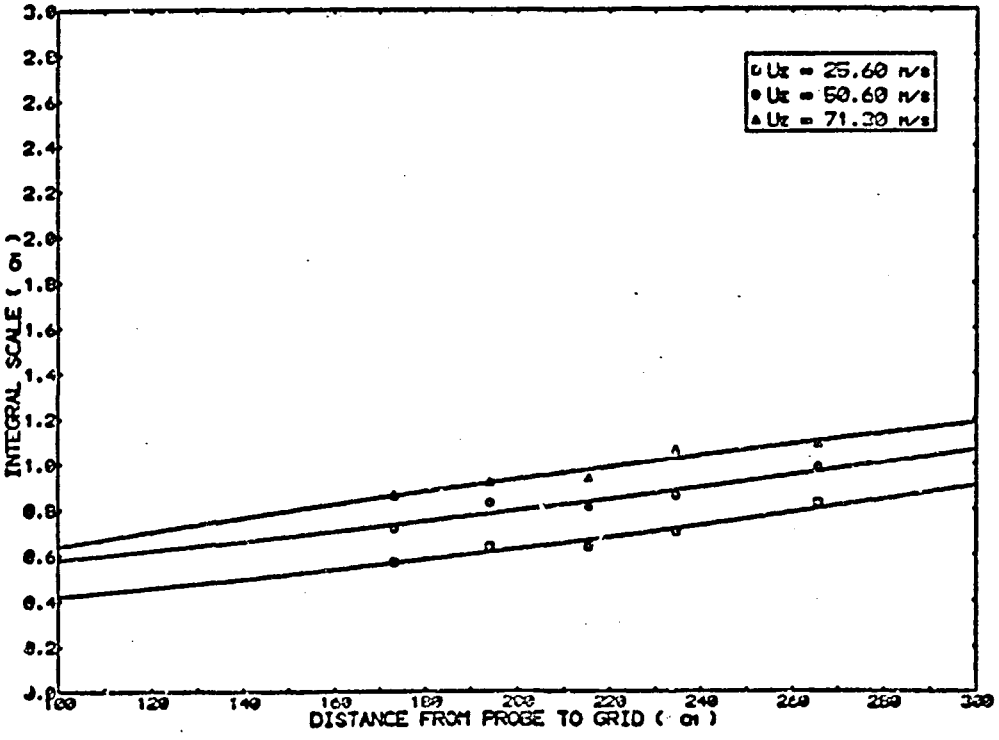

Fig. 7. Integral Scale in 41-cm Test Section (10.16-cm grid).

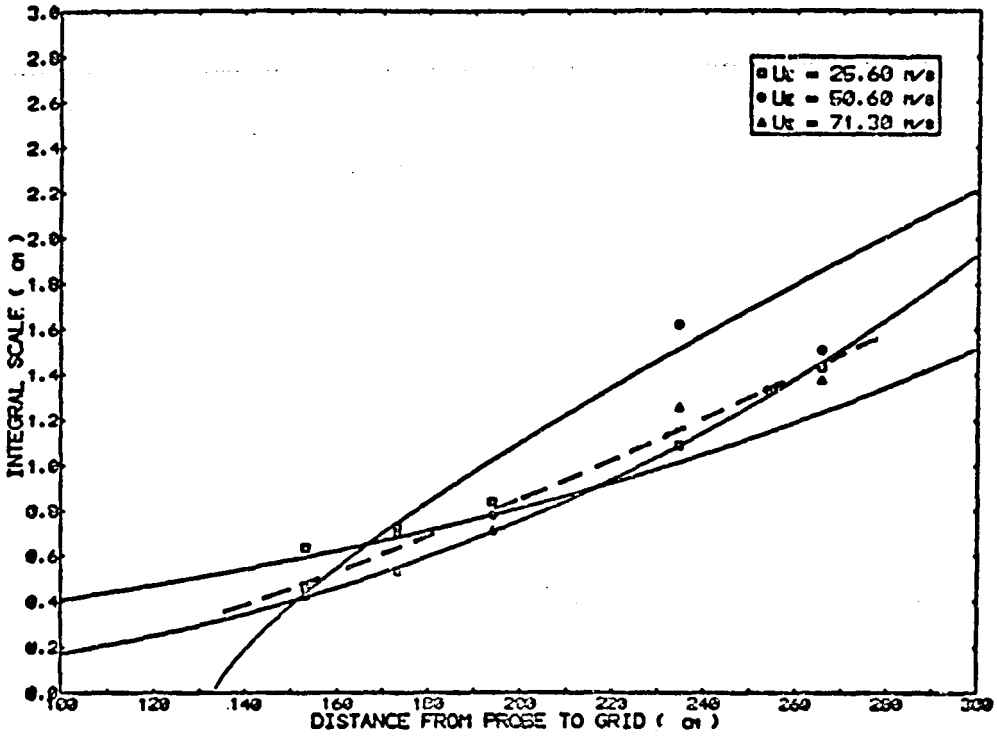

Fig. 8. Integral Scale in 41-cm Test Section (5.08-cm Grid).

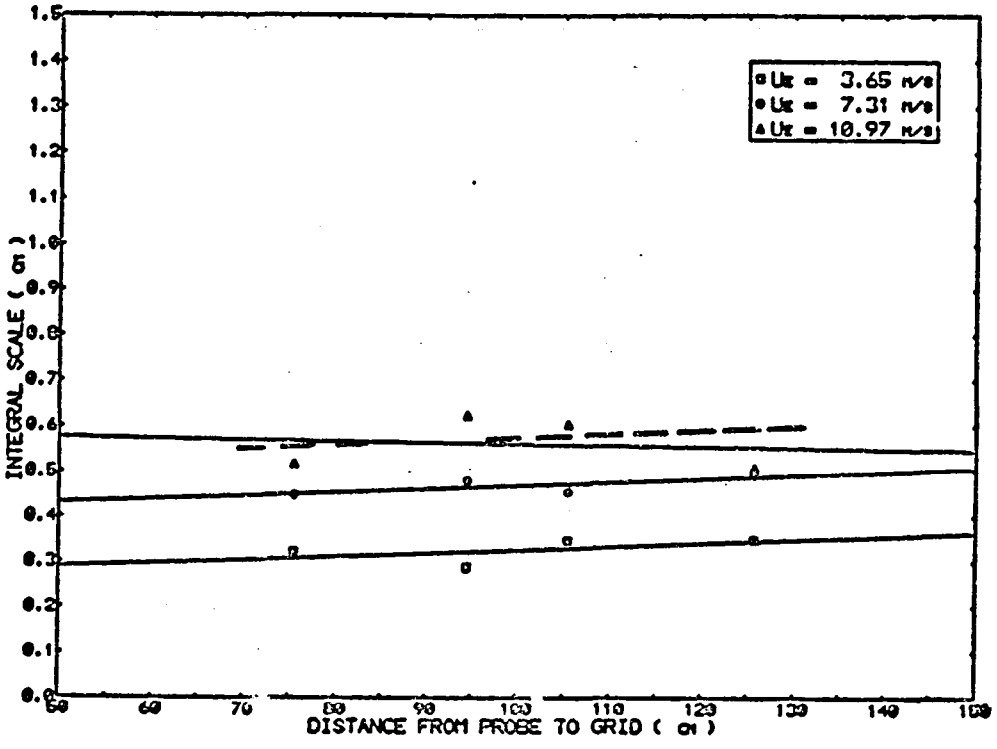

Fig. 9. Integral Scale in 102-cm Test Section (10.16-cm Grid).

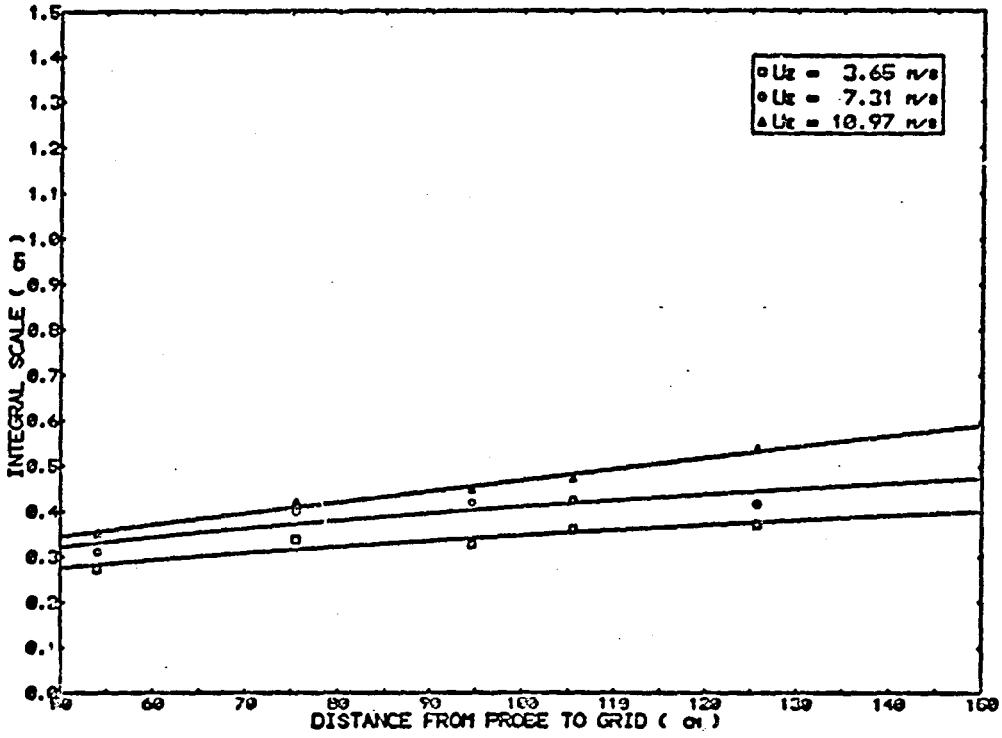

Fig. 10. Integral Scale in 102-cm Test Section (5.08-cm Grid).

ORIGINAL PAGE IS
OF POOR QUALITY

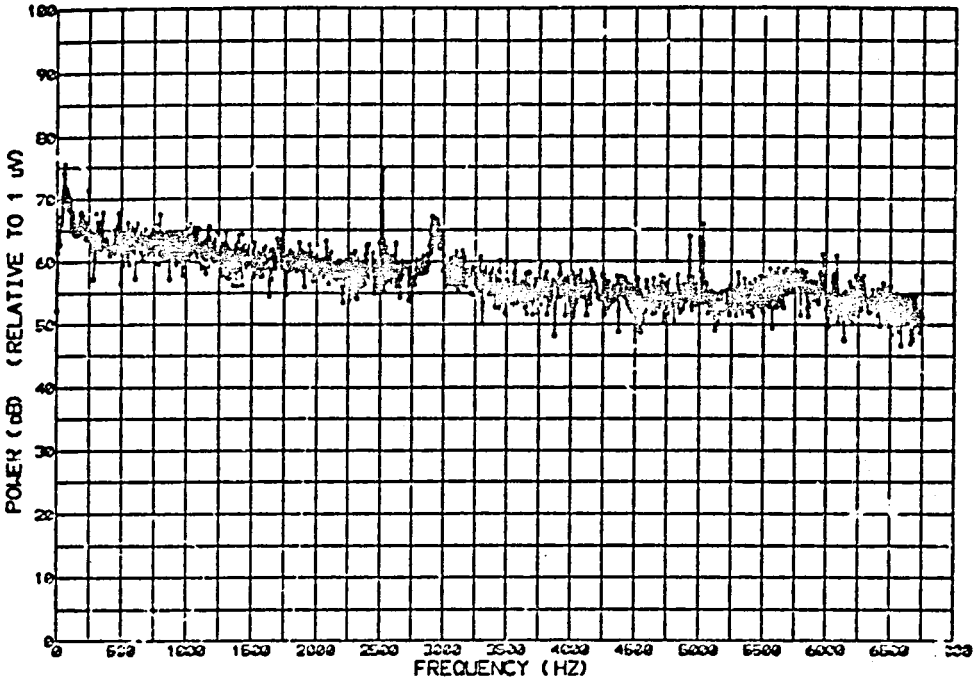

Fig. 11. Power Spectrum for 5.08-cm Grid at 234.5 cm.

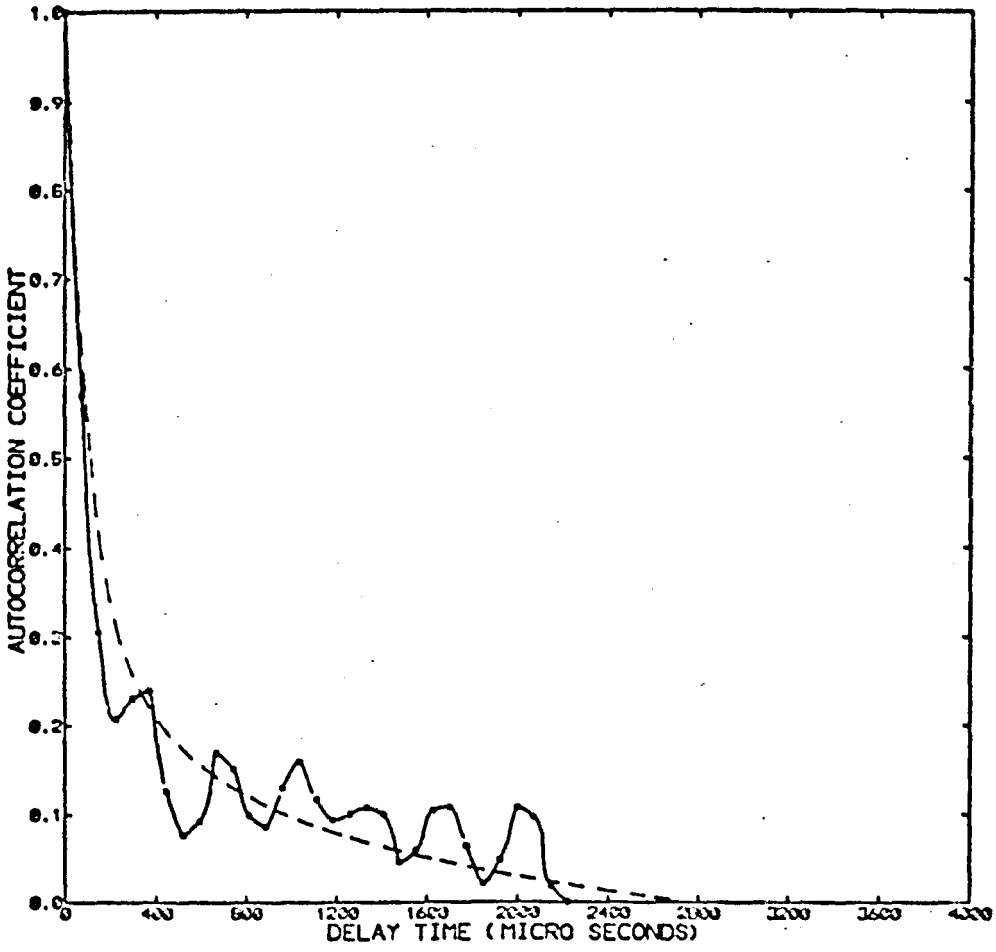

Fig. 12. Autocorrelation for 5.08-cm Grid at 234.5 cm.

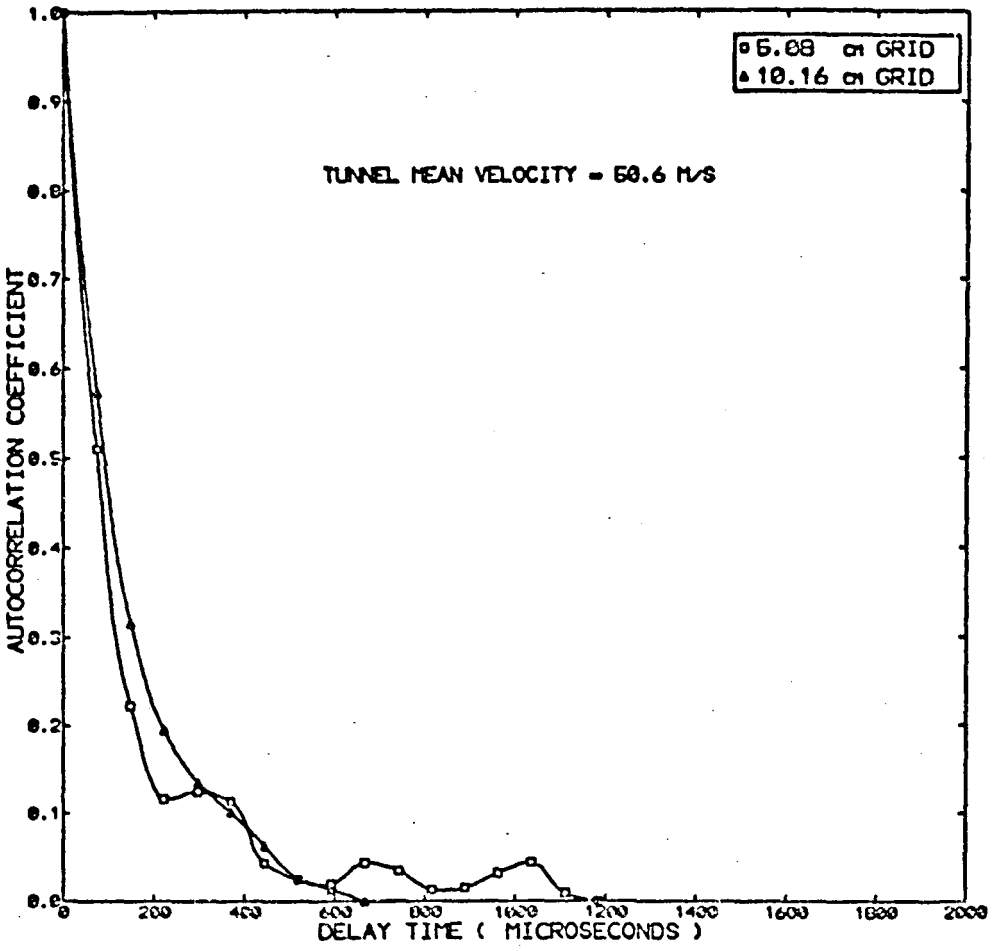

Fig. 13. Autocorrelation Function at Position 173.2 cm.

ORIGINAL PAGE IS
OF POOR QUALITY

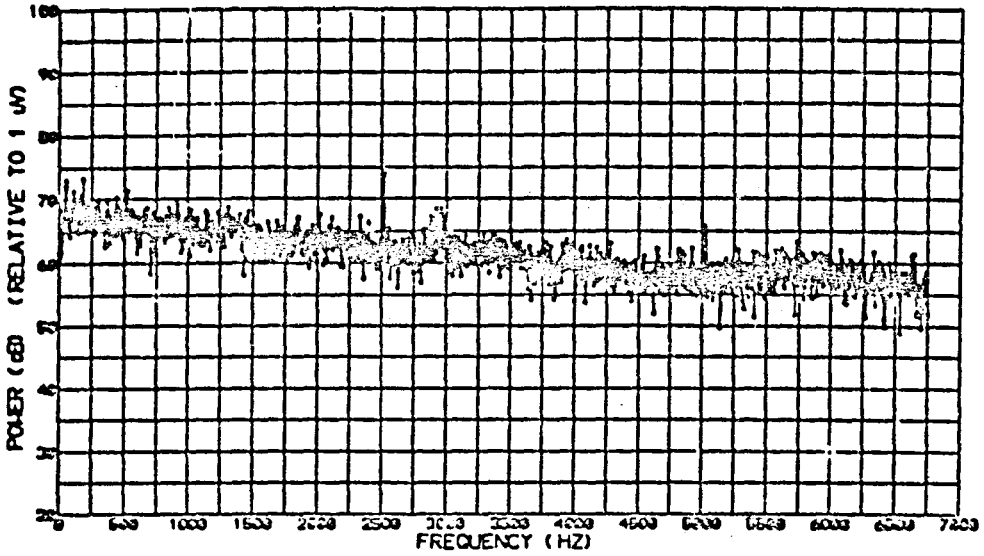

(a). 5.08-cm-mesh Grid.

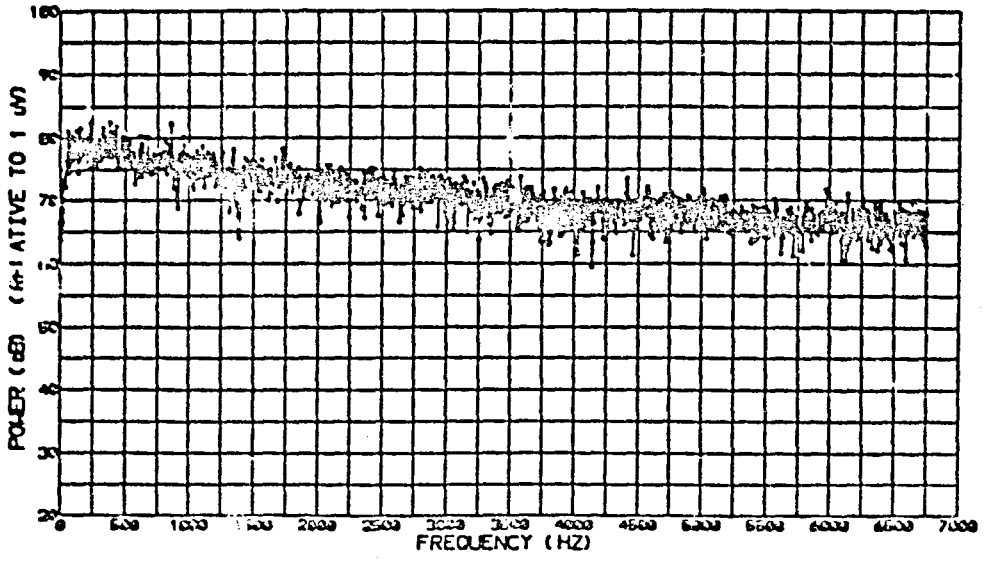

(b). 10.16-cm-mesh Grid.

Figure 14. Power Spectrum at position 173.2 cm.

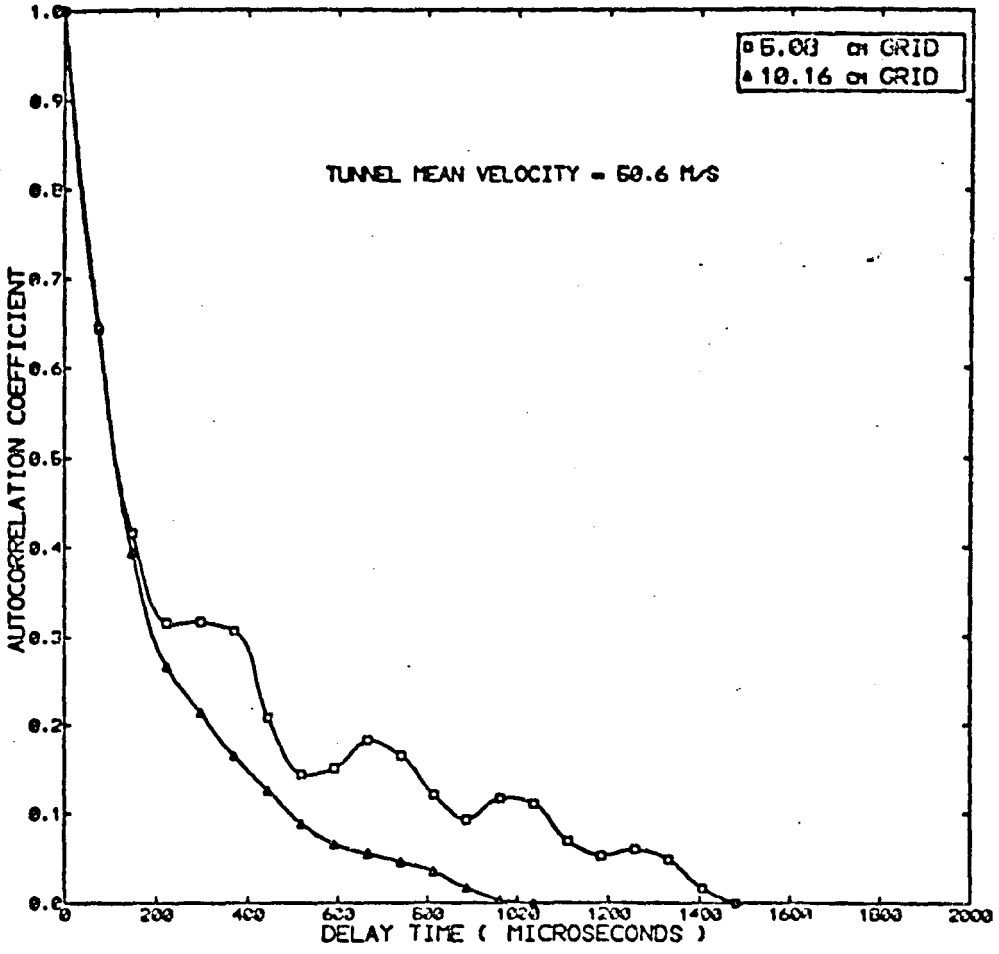

Fig. 15. Autocorrelation Function at Position 265.7 cm.

ORIGINAL PAGE IS
OF POOR QUALITY

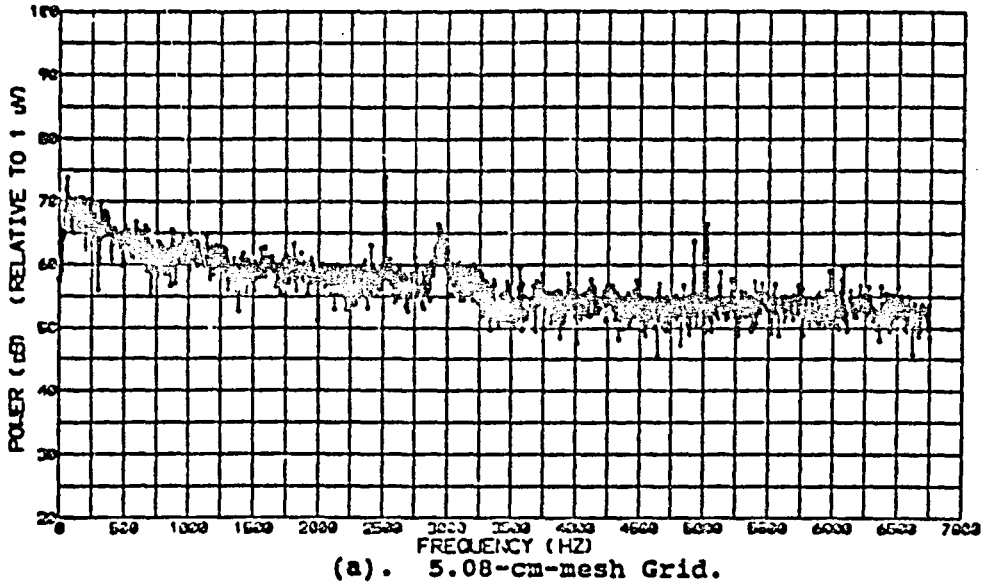

(a). 5.08-cm-mesh Grid.

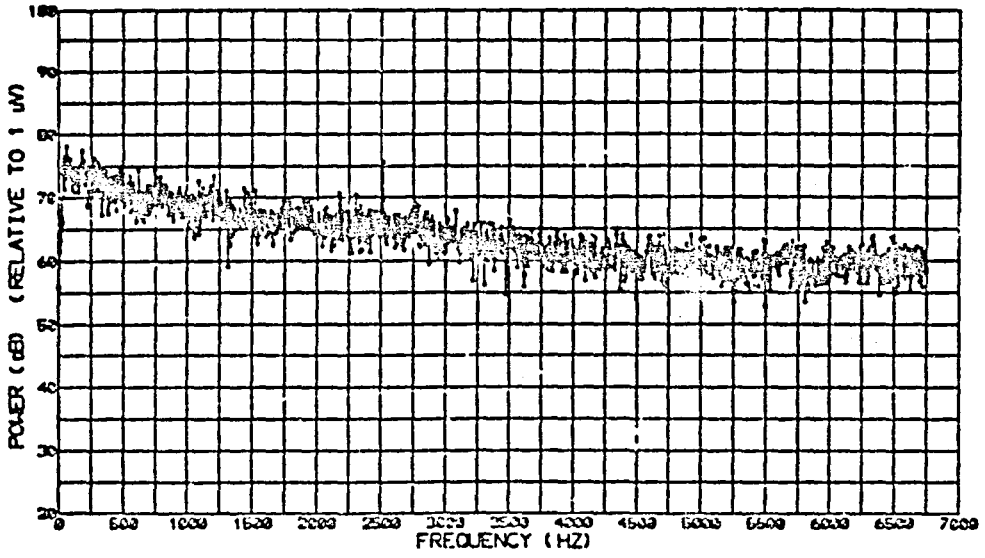

(b). 10.16-cm-mesh Grid.

Fig. 16. Power Spectrum at Position 265.7 cm.

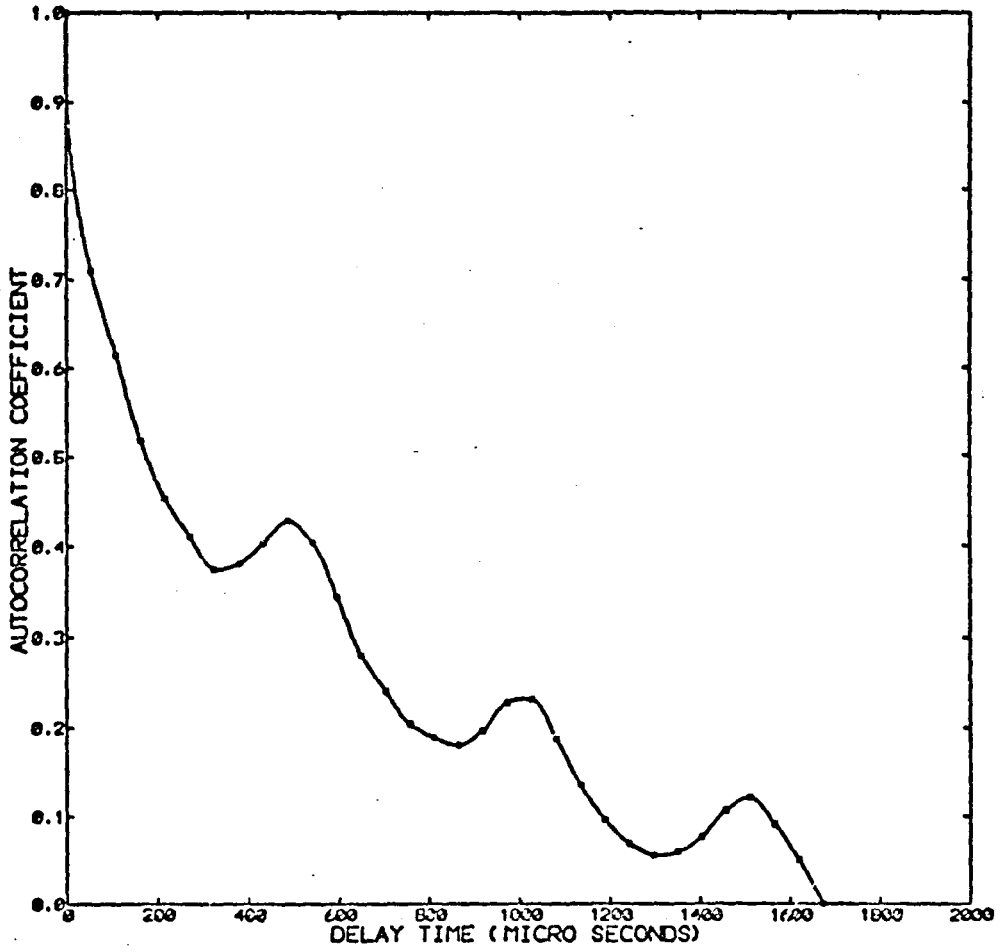

Fig. 17. Autocorrelation Function with no Grid.

ORIGINAL
OF POOR

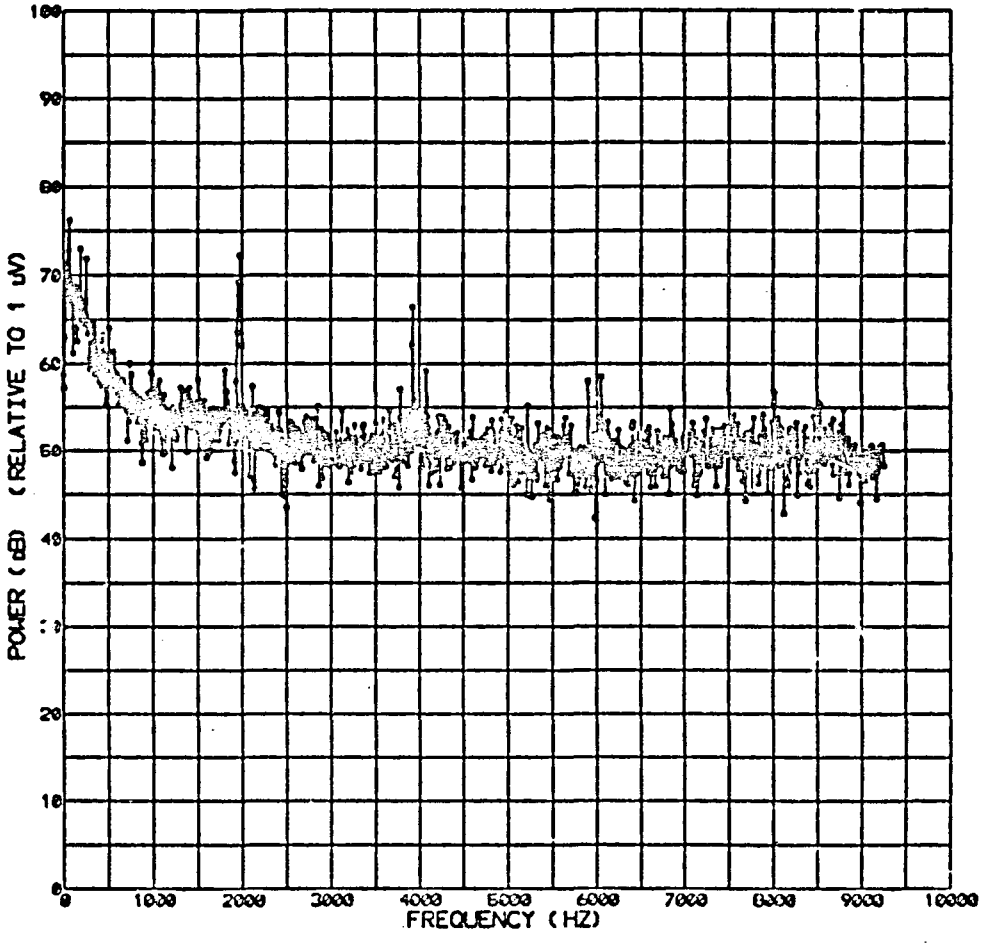

Fig. 18. Power Spectrum with no Grid.

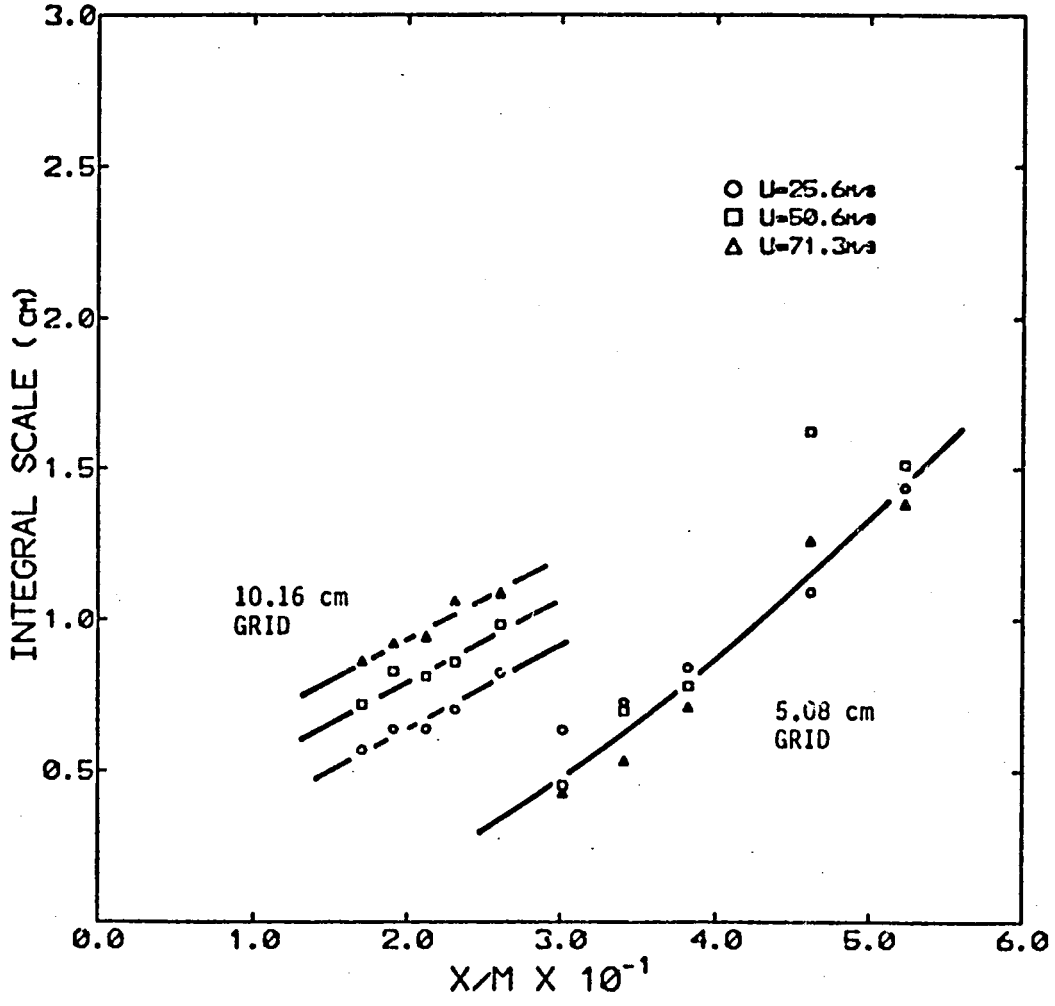

Figure 19. Integral Scale as a function of X/M

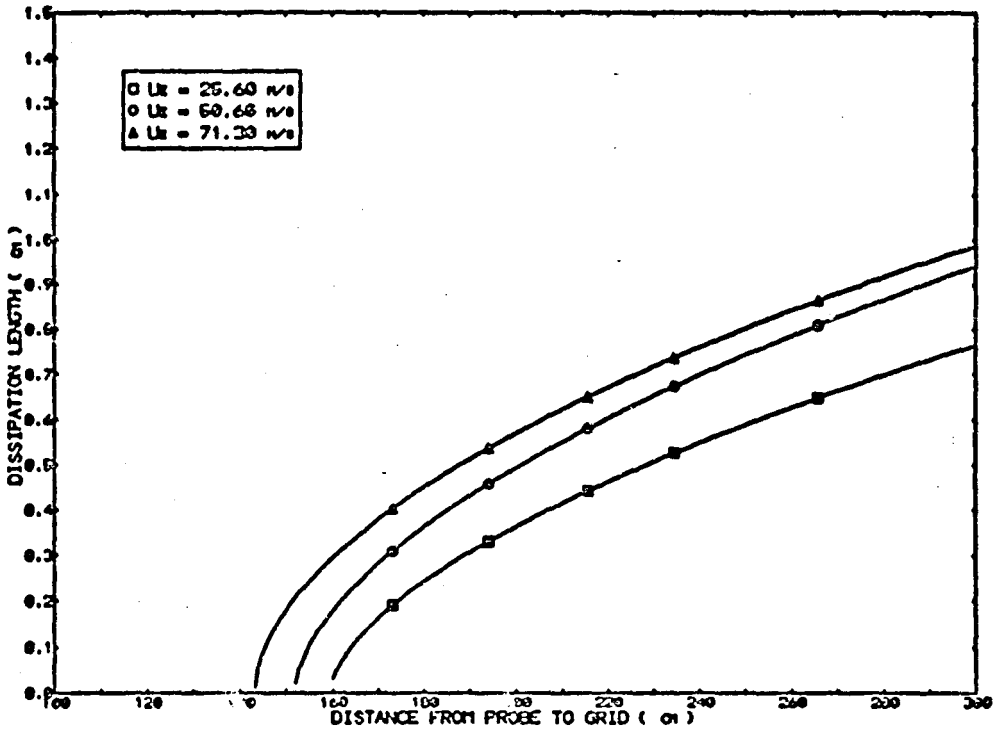

Fig. 20. Dissipation Length Parameter in 41-cm Test Section (10.16-cm Grid).

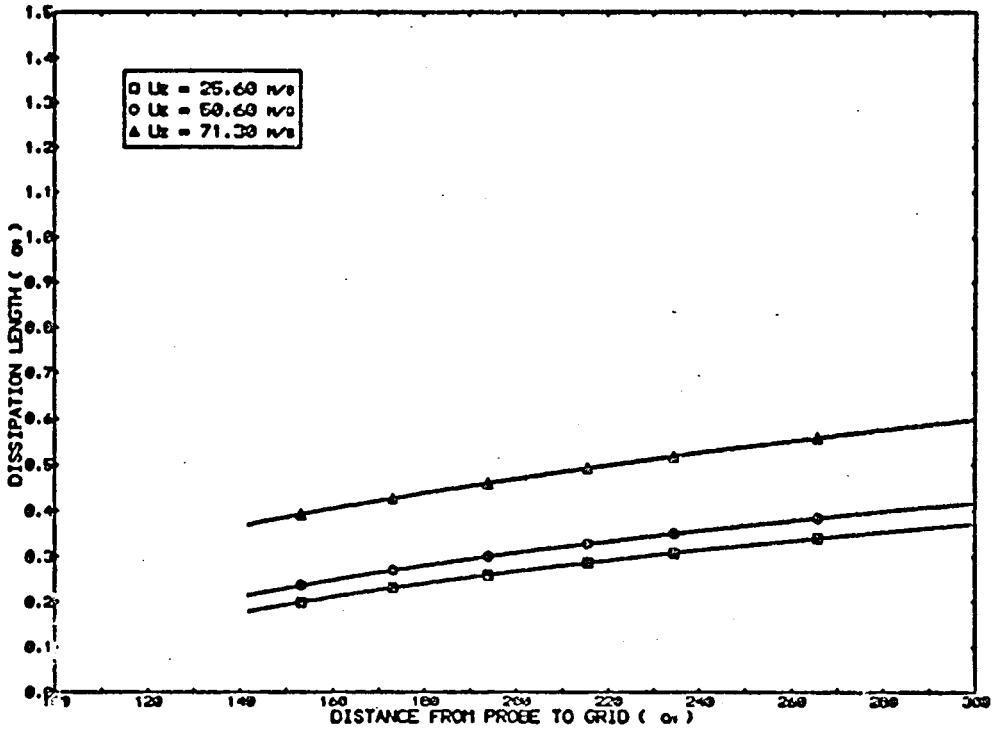

Fig. 21. Dissipation Length Parameter in 41-cm Test Section (5.08-cm Grid).

ORIGINAL PAGE IS
OF POOR QUALITY

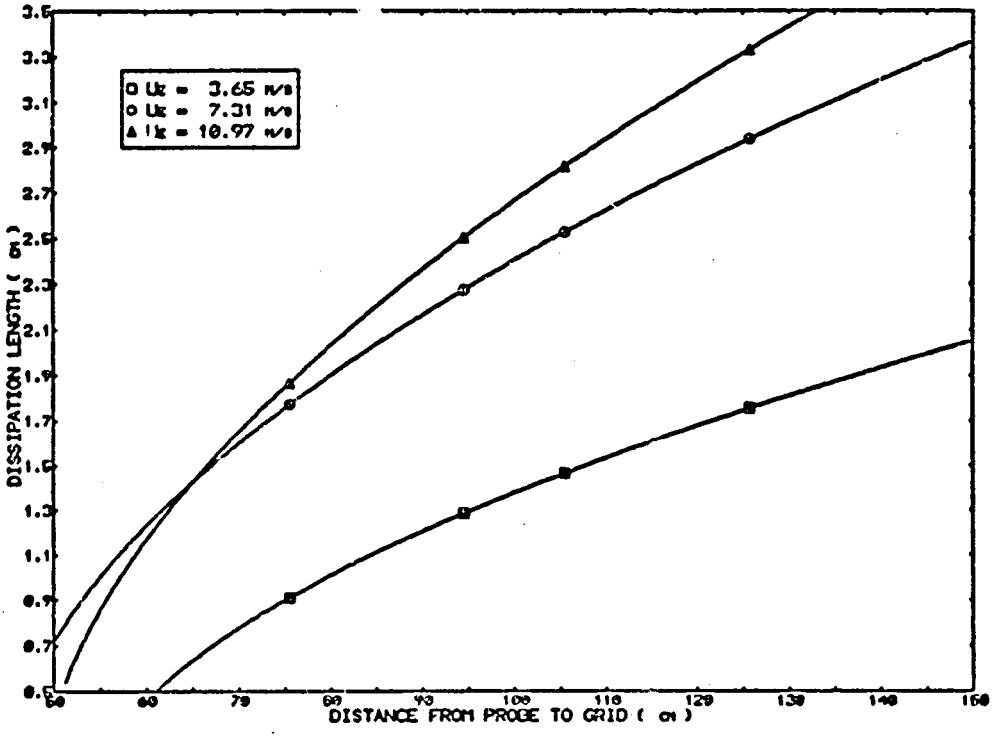

Fig. 22. Dissipation Length Parameter in 102-cm Test Section (10.16-cm Grid).

ORIGINAL PAGE IS
OF POOR QUALITY

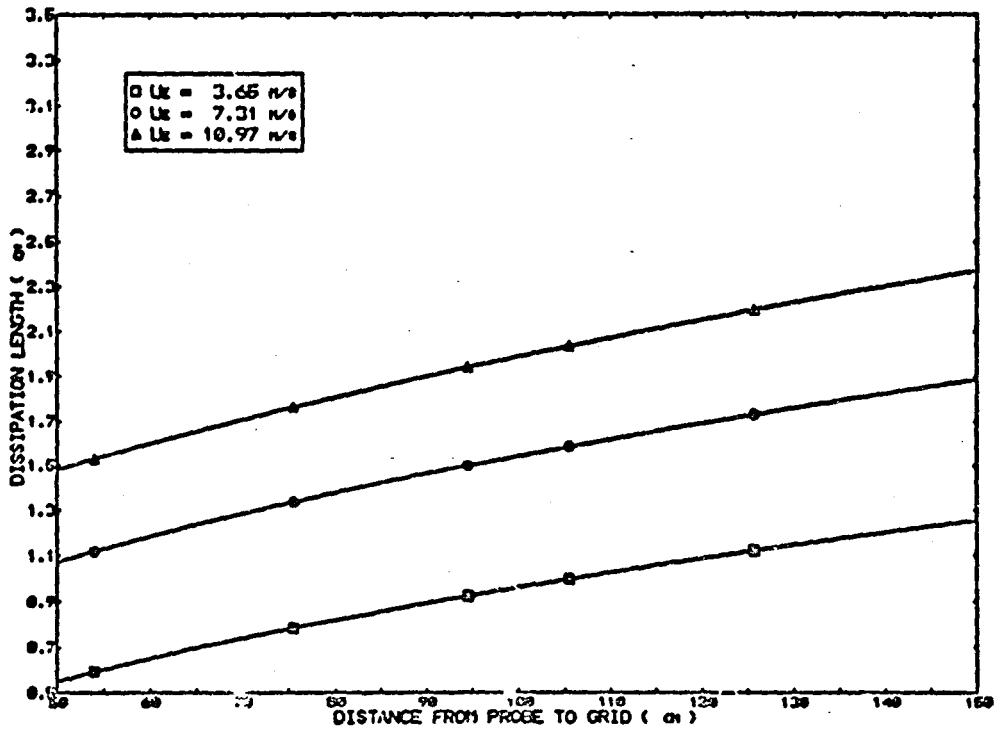

Fig. 23. Dissipation Length Parameter in 102-cm Test Section (5.08-cm Grid).

ORIGINAL PAGE IS
OF POOR QUALITY

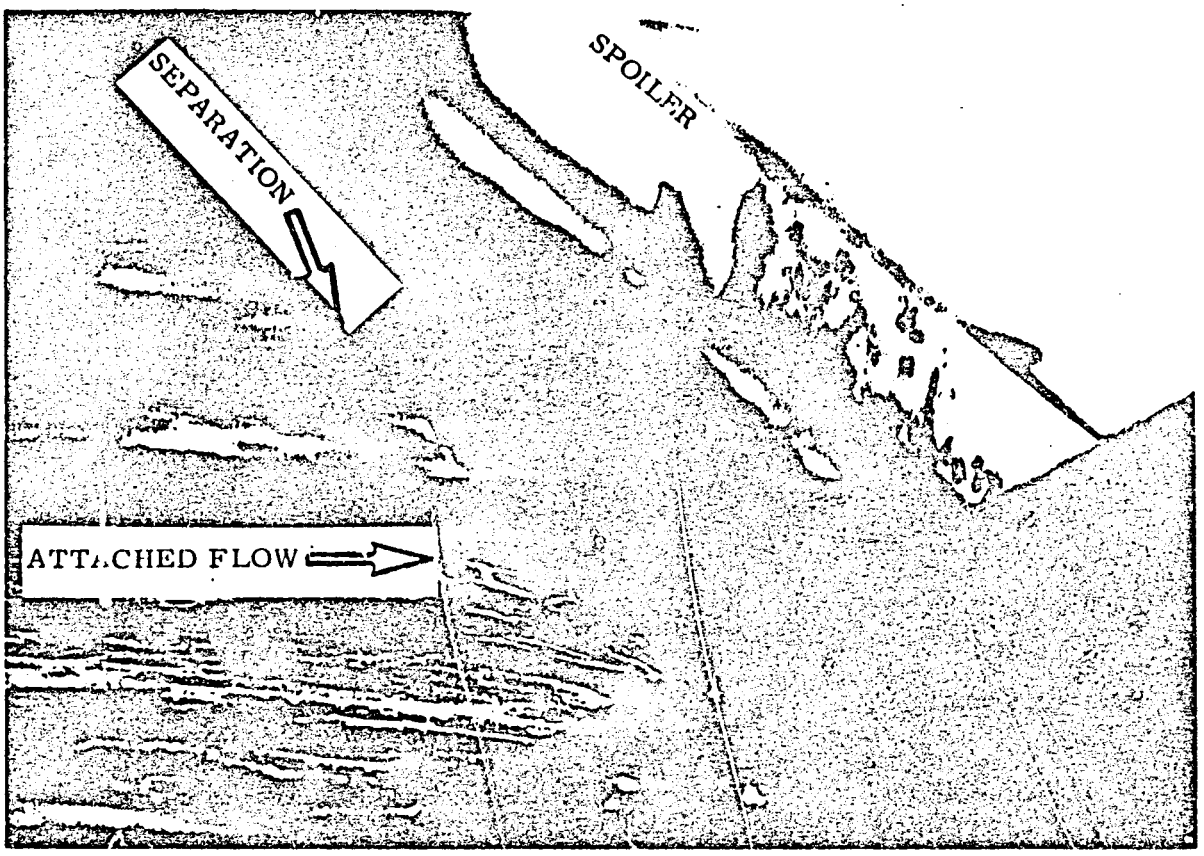

Figure 24. Spoiler and Surface Film Pattern.

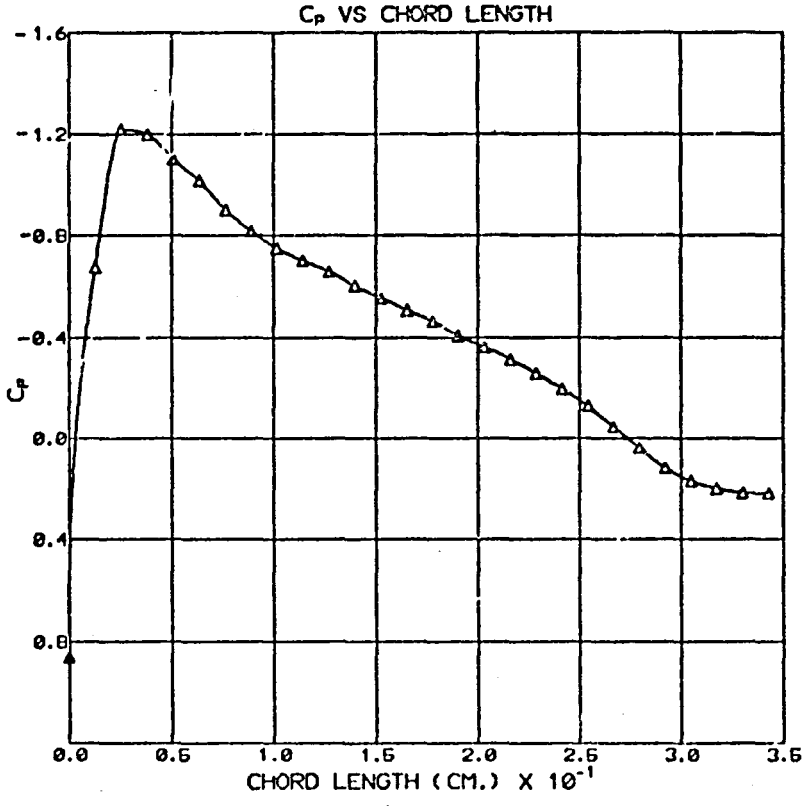

Figure 25. Upper Surface Pressure Coefficient.

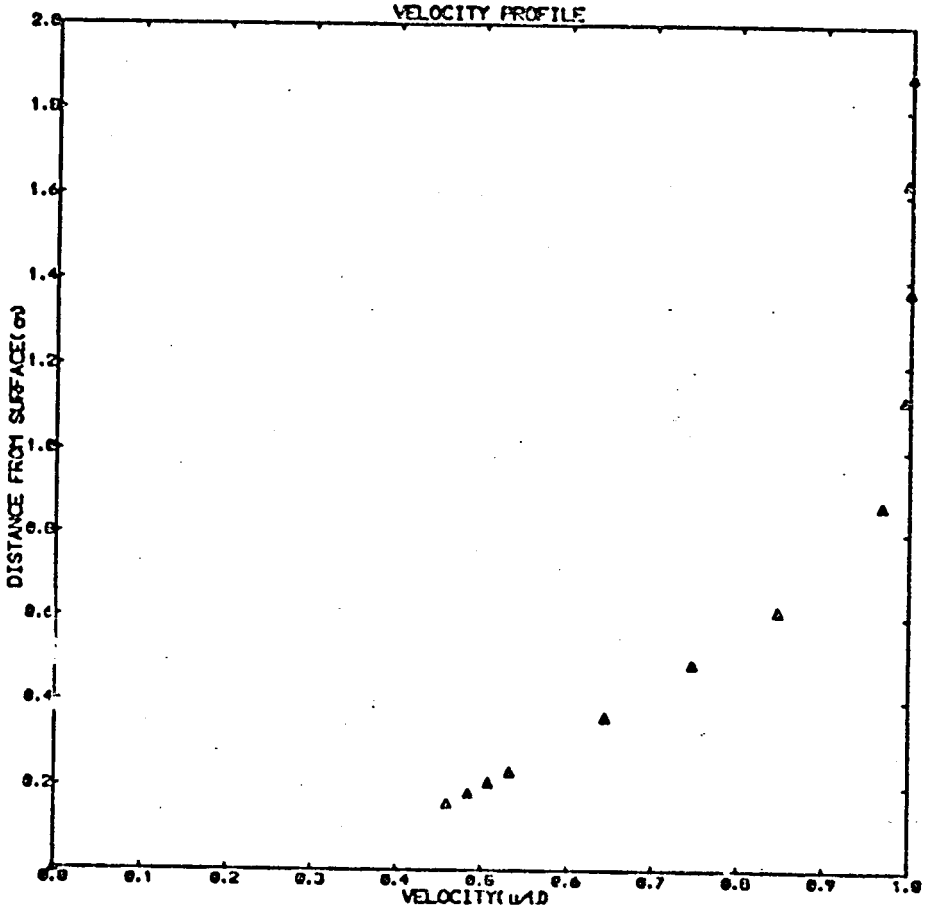

Figure 26. Boundary Layer Velocity Profile

END

DATE

FILMED

DEC 10 1985

End of Document